Engineering Applications of Artificial Intelligence 152 (2025) 110789

Contents lists available at ScienceDirect

Engineering Applications of Artificial Intelligence

journal homepage: www.elsevier.com/locate/engappai

Adaptive self-evolving extreme learning machine-based terminal sliding mode control with application in retinal vein injection

Bo Hu [a,b], Shiyu Xu [a,b], Lu Liu [c], Rongxin Liu [a,b], Mingzhu Sun [a,b], Xin Zhao [a,b,*]

[a] National Key Laboratory of Intelligent Tracking and Forecasting for Infectious Diseases, Engineering Research Center of Trusted Behavior Intelligence, Ministry of Education, Tianjin Key Laboratory of Intelligent Robotics, Institute of Robotics and Automatic Information System, Nankai University, Tianjin, 300350, China
[b] Institute of Intelligence Technology and Robotic Systems, Shenzhen Research Institute of Nankai University, Shenzhen, 518083, China
[c] Beijing Engineering Research Center of Industrial Spectrum Imaging, School of Automation and Electrical Engineering, University of Science and Technology Beijing, Beijing, 100083, China

ARTICLE INFO

Keywords:
Retinal vein injection
Neural networks
Extreme leaning machine
Self-evolving mechanism
Terminal sliding mode control

ABSTRACT

Retinal vein occlusion (RVO) is a serious condition that can lead to blindness. Injecting drugs into the retinal vein is a promising procedure for treating RVO. Due to the fragility of the retinal tissue, maintaining a precise drug flow rate (DFR) with a fast response is critical. Considering the unknown disturbance from piston dynamic and the drug-vein interaction, an adaptive self-evolving neural terminal sliding mode (ASNTSM) controller is proposed for DFR tracking. The integral terminal sliding surface is adopted to track the desired DFR in finite-time. The extreme learning machine (ELM) is utilized to estimate overall disturbances, and the adaptive switching gain is employed to compensate for the estimation error without requiring prior bounds. To achieve a compact ELM structure, a self-evolving mechanism is designed to implement the growth or pruning strategy of the hidden neurons. Theoretical analysis has proven that the ASNTSM controller can guarantee finite-time stability. Comparative experiments are conducted using a silicon phantom with simulated blood flow disturbances. The experimental results illustrate that the ASNTSM controller not only achieves lower transient time and average steady-state error, but also exhibits lower fluctuation and chattering effect. The self-evolving mechanism enhances the practicability of neural network in artificial intelligence-based medical engineering. Therefore, the ASNTSM controller is suitable for retinal vein injection tasks to improve surgical efficiency.

1. Introduction

Currently, humans are confronted with a variety of retinal diseases, including retinal injury, fundus hemorrhage, and macular edema, all of which significantly impact the quality of life (Laouri et al., 2011). Retinal vein occlusion (RVO) is a prevalent retinal disease that can induce significant visual impairment and, in some cases, complete loss of vision (Rogers et al., 2010). The treatment of RVO often involves retinal vein cannulation (RVC), a surgical procedure that requires accurate and stable drug injection into the retinal vein, as illustrated in Fig. 1. Specifically, the procedure involves manipulating a needle to rotate around the scleral incision to reach the retina. Once aligned with the target vein, the surgeon pierces the vein wall, injects the drug, and then withdraws the needle to complete the operation (Gerber et al., 2021). This surgical procedure typically relies on high-precision surgical tools and the skill of experienced surgeons, resulting in increased treatment costs. Consequently, the surgery is not yet widely adopted and remains largely in the research phase, with only a limited number of clinical cases reported (Willekens et al., 2017, 2021).

In the process of RVC surgery, the drug flow rate (DFR) directly impacts the efficiency and safety of the procedure. Precise control of DFR ensures effective injection volumes and minimizes potential damage to the patient (Zhang et al., 2023). Rapid tracking of DFR can also reduce the duration of RVC surgery. Therefore, ensuring a fast and

* Corresponding author. National Key Laboratory of Intelligent Tracking and Forecasting for Infectious Diseases, Engineering Research Center of Trusted Behavior Intelligence, Ministry of Education, Tianjin Key Laboratory of Intelligent Robotics, Institute of Robotics and Automatic Information System, Nankai University, Tianjin, 300350, China.

E-mail addresses: hubo@mail.nankai.edu.cn (B. Hu), 2120220529@mail.nankai.edu.cn (S. Xu), d202110338@xs.ustb.edu.cn (L. Liu), 2120230484@mail.nankai.edu.cn (R. Liu), sunmz@nankai.edu.cn (M. Sun), zhaoxin@nankai.edu.cn (X. Zhao).

https://doi.org/10.1016/j.engappai.2025.110789
Received 26 August 2024; Received in revised form 23 February 2025; Accepted 3 April 2025
Available online 11 April 2025

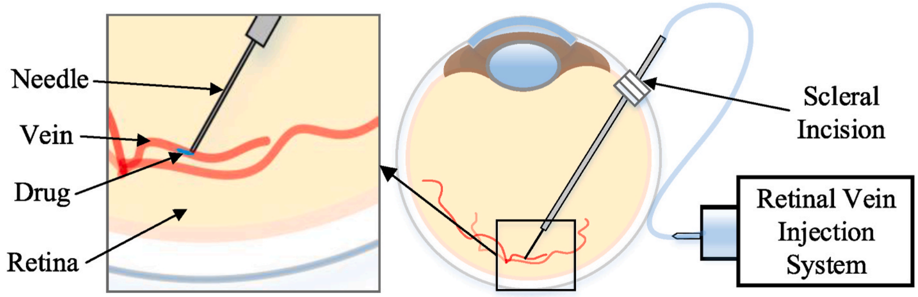

Fig. 1. Retinal vein injection process.

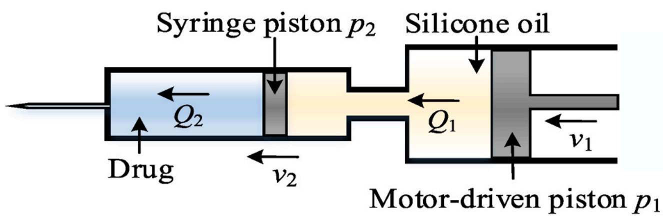

Fig. 2. The diagram of the retinal vein injection system.

precise DFR is crucial, and it requires a reliable retinal vein injection system to achieve these performance goals. Vitreous cutting machine is a typical instrument used in retinal surgery (Kitagawa et al., 2023). Its injection module relies on air pressure to deliver drugs into the subretina or retinal vein lumen. However, the compressibility of air reduces the stability of DFR, making it difficult to mitigate the risk of retinal tissue damage (Xu et al., 2024). Moreover, the vitreous cutting machine has a low degree of automation and lacks DFR feedback, which cannot guarantee consistent injection performance. To address these limitations, Xu et al. (2024) designed a silicone oil-driven retinal vein injection system. In this system, a motor provides a stable driving force for drug injection. The addition of silicone oil not only buffers the motor's chattering but also enables DFR feedback. Consequently, this type of retinal vein injection system is expected to provide fast and precise DFR control with reliable feedback, thereby enhancing surgical outcomes.

Achieving fast and precise control of the drug flow rate (DFR) is challenging due to disturbances from the syringe piston and retinal tissue (Kim et al., 2019). As illustrated in Fig. 2, the silicone oil-driven retinal vein injection system lacks a rigid connection between the syringe piston and the motor-driven piston. During the start-up phase, the syringe piston must overcome unknown friction, leading to significant overshoot (Kim et al., 2019; Xu et al., 2024). This overshoot can shock the retinal vein tissue, potentially causing mechanical damage and increasing the risk of bleeding. In addition to unknown piston friction, drug-vein interactions introduce further disturbances to DFR control at the microscopic level (Wu et al., 2013). In clinical applications, obtaining prior knowledge of drug-vein interactions is difficult and relies on extensive clinical data, making modeling both complex and costly. These disturbances not only affect the rapidity of DFR tracking but also increase tracking errors, which are unacceptable in clinical RVC surgery. Moreover, the long transient time associated with overshoot degrades the fast response of the DFR, potentially prolonging the duration of RVC surgery. Based on this analysis, designing a high-precision, robust controller with a fast response to unknown disturbances is a key motivation of this study.

Given the presence of unknown nonlinear disturbances in retinal vein injection systems, traditional control methods (such as proportional–integral–derivative control) struggle to achieve satisfactory control performance. To address control challenges across various fields, numerous advanced control strategies have been proposed, including adaptive control (Annaswamy et al., 2023), model predictive control (MPC) (Fei and Liu, 2021), intelligent control (Fei et al., 2021), and sliding mode control (Utkin et al., 2020). Adaptive control and MPC rely on precise system dynamics, and the disturbances encountered in retinal vein injection system can limit their applicability. Intelligent control, a data-driven approach, is well-suited for handling uncertain and nonlinear systems. Among these, the neural network (NN) controller stands out for its ability to approximate nonlinear factors effectively. The NN controller can theoretically ensure the convergence of tracking and approximation errors (Fei et al., 2021). However, considering the clinical requirements of RVC, relying solely on NN controller is insufficient to simultaneously achieve both rapidity and precision. It is well known that sliding mode (SM) controllers offer strong robustness and high control accuracy (Utkin et al., 2020). However, SM controller can only theoretically guarantee the asymptotic convergence of the closed-loop system to zero, which does not meet the fast response requirements for DFR control. Terminal sliding mode (TSM) controller, as an improvement over SM controllers, enhance convergence speed (Dong et al., 2022). In the medical field, fast-response control systems have significant clinical benefits. In Feng et al. (2022), an adaptive integrated terminal sliding mode force controller was designed for ear surgery, achieving higher tracking performance. In Fuentes-Alvarez et al. (2022), a strategy combining recurrent NN and adaptive non-singular fast terminal sliding mode controller was used to control the trajectories of an exoskeleton, offering both accuracy and intelligence. However, these medical applications typically prioritize precision over response speed, which is not suitable for DFR control that requires a fast response. Additionally, the discontinuous control law of TSM controller can produce control chattering, particularly due to the lack of inherent disturbance-rejection mechanism. This phenomenon has the potential to shorten the lifespan of the retinal vein injection system.

Given the advantages of TSM controller in terms of convergence speed and tracking accuracy, combining TSM controllers with observers is expected to enhance robustness and reduce chattering. Model-based observers, such as disturbance observer (Ding et al., 2020), sliding mode observer (Wang et al., 2022), and extended state observer (Zhang et al., 2021), are widely used in control applications. These observers rely on prior knowledge of system dynamics and are suitable for constant disturbances. However, DFR control faces uncertainties in piston friction and unknown drug-vein interactions. Furthermore, during different stages of retinal vein injection, disturbances caused by piston friction primarily occur during the start-up phase, while disturbances from drug-vein interactions affect dynamic performance after the start-up phase. These varying and unknown nonlinear disturbances limit the estimation performance of model-based observers. It is feasible to use NN as an auxiliary technology to estimate unknown disturbance without prior knowledge (Liu et al., 2020). Compared to model-based observers, the combination of TSM controller and NN observer is more suitable for retinal vein injection. This framework can leverage the approximation capabilities of NNs and is expected to compensate for unknown nonlinear disturbances while ensuring accuracy and rapidity (Hou et al., 2024a). Among widely used NN estimators, the extreme learning machine (ELM) is known for its simple structure and fast training speed (Huang et al., 2015; Berghout et al., 2020; Wu et al., 2023). In practice, the hidden layer size of ELM primarily affects the performance. Determining the structure based on manual experience is limited in improving control precision. For DFR control, ELM with a fixed structure struggles to adapt to varying disturbances. Excess neurons increase computational complexity, while insufficient neurons make it difficult to estimate complex disturbances accurately. Although intelligent algorithms can achieve structural optimization, results based on historical data cannot adapt to varying clinical scenarios (Xia et al., 2022). Currently, self-evolving mechanisms offer a way to obtain compact structures with better performance (Fei et al., 2022a,b; Hou et al., 2024b). In Fei et al. (2022a), a self-evolving recurrent Chebyshev fuzzy NN approximator combined with a fractional-order SM controller was designed for an active power filter to suppress harmonic distortions. The NN approximator in this study can achieve structure updating without predefined neurons. Although self-evolving mechanisms have demonstrated effectiveness in other studies, their application in ELM is restricted due to its unique architectural characteristics. Since the input weights of ELM are fixed, self-evolving mechanisms designed for other networks, such as fuzzy NNs or broad networks, cannot be directly applied to ELM estimators (Fei et al., 2022b; Han et al., 2024). From a control system perspective, changes in the hidden structure can affect closed-loop stability (Chen and Dong, 2024; Ding et al., 2024). This makes the design of a self-evolving mechanism for control tasks different from that for classification or prediction tasks. In addition, although the NN estimator can reduce chattering by employing a lower switching gain, its inherent approximation error cannot be ignored. A fixed switching gain is insufficient to effectively compensate for this approximation error. To enhance tracking precision in the presence of disturbances, it is crucial to design a self-evolving mechanism specifically tailored for the ELM and to implement an adaptive switching gain for DFR control.

In light of the aforementioned challenges associated with retinal vein injection, it is imperative to develop a control strategy that achieves both high precision and rapid response while remaining robust to varying nonlinear disturbances. To this end, an adaptive self-evolving neural terminal sliding mode (ASNTSM) control scheme is proposed for DFR control. Specifically, a composite control framework is designed by integrating a TSM controller with an ELM estimator. Moreover, an adaptive gain law and a self-evolving mechanism are developed to dynamically update the switching gain and hidden layer structure, respectively. The main contributions of this paper are as follows.

1) Given the stringent temporal and precision requirements of RVC surgery, achieving rapid and precise tracking control of the DFR is of paramount importance. TSM control is selected as the fundamental strategy to enhance the convergence speed and tracking accuracy of the DFR. Thanks to the TSM surface, the proposed ASNTSM controller can theoretically achieve finite-time stability while maintaining robustness, which is a significant improvement over traditional SM control.
2) To address the unknown piston dynamics and drug-vein interaction disturbances in DFR control, the ELM is employed to compensate for these unknown nonlinear disturbances. The goal is to further improve tracking accuracy while reducing chattering. Compared to model-based observers, the ELM is chosen for its superior nonlinear approximation capability and simple structure, making it well-suited for deployment in the retinal vein injection system.
3) To cope with the characteristics of varying disturbances, two adaptive laws are designed. A self-evolving mechanism is proposed to enable online structure updating of the ELM. This customized mechanism, based on tracking error and defined neuron importance, achieves the growth or pruning of hidden neurons. Theoretical analysis demonstrates that this self-evolving mechanism does not affect closed-loop stability. Additionally, an adaptive switching gain is employed to compensate for the estimation error of the ELM. The adaptive switching gain theoretically avoids overestimation and further reduces the chattering. Compared to fixed estimator and fixed switching gain, the ASNTSM controller has the ability to adapt to varying disturbances in DFR control.

The remainder of this article is organized as follows. The retinal vein injection system modeling is described in Section 2, along with fundamental knowledge of ELM. The ASNTSM controller, self-evolving mechanism, stability analysis, and guidelines for parameter selection are delineated in Section 3. Experiments are carried out in Section 4 to verify the efficacy of ASNTSM controller in various simulated blood flow disturbances. Section 5 serves as the conclusion.

2. Problem formulation

2.1. Retinal vein injection system modeling

The structure of the retinal vein injection system is shown in Fig. 2. In this system, a motor-driven piston propels silicone oil, which in turn drives the syringe piston to deliver the drug fluid. Given the elastic properties of the rubber piston, the dynamics of the silicone oil flow can be modeled as a first-order system. (Kim et al., 2019; Xu et al., 2024).

$$A_1\dot{Q}_1 + B_1Q_1 = v_1 + d_1 \tag{1}$$

where Q_1 and $\dot{Q}_1$ represent the flow rate of the silicone oil and its first derivative, respectively. v_1 denotes the velocity of the motor-driven piston p_1. d_1 denotes the unknown disturbance. A_1 and B_1 are positive parameters. For the syringe, disregarding the effects of pressure changes, silicone oil leakage, and piston friction, the relationship between the velocity of the syringe piston v_2 and the DFR Q_2 is simplified as (Helian et al., 2022):

$$Q_2 = Sv_2 + d_0 \tag{2}$$

where S denotes the inner area of the syringe piston p_2. d_0 denotes the unknown disturbance. Similar to Eq. (1), the dynamics of DFR Q_2 can be obtained as:

$$A_2\dot{Q}_2 + B_2Q_2 = v_2 + d_2 \tag{3}$$

where Q_2 and $\dot{Q}_2$ represent the DFR and its first derivative, respectively. v_2 denotes the velocity of the syringe piston p_2. d_2 denotes the modeling uncertainty, primarily caused by the elasticity of the rubber. A_2 and B_2 are positive parameters. Based on Eqs. (1)–(3), the following second-order dynamics can be obtained.

$$A_1A_2S\ddot{Q}_2 + S(A_1B_2 + A_2B_1)\dot{Q}_2 + B_1B_2SQ_2 = v_1 + d_Q \tag{4}$$

where $\ddot{Q}_2$ denotes the second derivative of the DFR Q_2, d_Q denotes the overall disturbance. Eq. (4) can be further simplified as:

$$\ddot{Q}_2 + a\dot{Q}_2 + bQ_2 = cv_1 + d \tag{5}$$

where $a = \frac{A_1B_2+A_2B_1}{A_1A_2}$, $b = \frac{B_1B_2}{A_1A_2}$, $c = \frac{1}{A_1A_2S}$, $d = \frac{1}{A_1A_2S}d_Q$. Select the state variable as $x = [x_1, x_2]^T = [Q_2, \dot{Q}_2]^T$ and control input as $u = v_1$, the system dynamics given by Eq. (5) can be rewritten as follows:

$$\begin{cases} \dot{x}_1 = x_2 \\ \dot{x}_2 = cu - ax_2 - bx_1 + d \end{cases} \tag{6}$$

The system parameters a, b and c are partially unknown, which can be expressed as $a = a_n + \Delta a$, $b = b_n + \Delta b$, and $c = c_n + \Delta c$, where a_n, b_n, and c_n are the nominal terms, and Δa, Δb, and Δc are the bias terms. We assume that the closed-loop control law u is upper bounded by $|u| < \mu_0$, where μ_0 is a positive constant. Therefore, the retinal vein injection system can be rewritten as:

$$\begin{cases} \dot{x}_1 = x_2 \\ \dot{x}_2 = c_n u - a_n x_2 - b_n x_1 + d_t \end{cases} \tag{7}$$

where $d_t = -\Delta a x_2 - \Delta b x_1 - \Delta c u + d$ denotes the lumped disturbance. We assume that the unknown bias term Δa, Δb, and Δc are continuous and bounded, i.e., $|\Delta a| \leq \overline{a}$, $|\Delta b| \leq \overline{b}$, $|\Delta c| \leq \overline{c}$, where $\overline{a}$, $\overline{b}$, and $\overline{c}$ are positive constants. The d is continuous and bounded by $|d| \leq \overline{d}$. Then the lumped disturbance d_t is upper bounded by:

$$\begin{aligned} |d_t| &\leq |\Delta a x_2| + |\Delta b x_1| + |\Delta c u| + |d| \\ &\leq (\overline{c}\mu_0 + \overline{d}) + \overline{b}|x_1| + \overline{a}|x_2|. \end{aligned} \tag{8}$$

Remark 1. The friction dynamics of the syringe piston are difficult to model directly, especially given the unobservable velocity of the syringe piston. Additionally, the unknown disturbances arising from drug-vein interactions cannot be explicitly incorporated into the above DFR dynamics. Therefore, a learning-based approach is necessary to estimate these overall unknown disturbances.

2.2. ELM

The single-layer feedforward network is widely recognized as one of the most common NN models, with backpropagation being the traditional method employed to optimize network weights. However, backpropagation, which relies on gradient descent, is known for its drawbacks, including slow learning speed and susceptibility to local minima. To address these limitations, the ELM method has been proposed as an alternative to backpropagation. The fast learning speed of ELM is attributed to its random generation of input weights and biases, which eliminates the need to iteratively train the output weights (Huang et al., 2015). In this section, a brief overview of the fundamentals of ELM is provided. For a given sample set (z_j, t_j), the outputs of the ELM approximator with N_h hidden nodes can be described by

$$\sum_{i=1}^{N_h} \beta_i G\left(w_i z_j + g_i\right) = t_j, j = 1, \cdots, N. \tag{9}$$

where $z_i = [z_{i1}, z_{i2}, \cdots, z_{im}]^{\mathrm{T}} \in \mathbb{R}^m$ is the input vector, $t_i = [t_{i1}, t_{i2}, \cdots, t_{in}]^{\mathrm{T}} \in \mathbb{R}^n$ is the output vector, $w_i = [w_{i1}, w_{i2}, \cdots, w_{im}]^{\mathrm{T}} \in \mathbb{R}^m$ is the input weight vector, g_i represents the bias of the hidden neurons, $\beta_i = [\beta_{i1}, \beta_{i2}, \cdots, \beta_{in}]^{\mathrm{T}}$ is the output weight vector connecting the i-th hidden neurons and the output neuron, and $G(\cdot)$ denotes the activation function. Subsequently, Eq. (9) can be further rearranged into the following form:

$$H\beta = T \tag{10}$$

where

$$H(z, w, g) = \begin{bmatrix} G(z_1, w_1, g_1) & \cdots & G\left(z_1, w_{N_h}, g_{N_h}\right) \\ \vdots & \cdots & \vdots \\ G(z_N, w_1, g_1) & \cdots & G\left(z_N, w_{N_h}, g_{N_h}\right) \end{bmatrix} \in \mathbb{R}^{N \times N_h}$$

denotes the hidden layer output matrix. The output weight matrix is $\beta = \left[\beta_1^{\mathrm{T}}, \beta_2^{\mathrm{T}}, \cdots, \beta_{N_h}^{\mathrm{T}}\right]^{\mathrm{T}} \in \mathbb{R}^{N_h \times n}$, and the output matrix $T = \left[t_1^{\mathrm{T}}, t_2^{\mathrm{T}}, \cdots, t_L^{\mathrm{T}}\right]^{\mathrm{T}} \in \mathbb{R}^{N \times n}$.

The ELM has the following property (Huang et al., 2015): For any small positive value ε_N, and an infinitely differentiable activation function $G(\cdot)$, there exists a number of the hidden neuron $N_h \leq N$ such that, for N arbitrary distinct samples (z_j, t_j), and for any input weight w and bias g selected from any intervals of $\mathbb{R}^m$ and $\mathbb{R}$, respectively, based on a continuous probability distribution, then with probability one:

$$\|H(z, w, g)\beta - T\| = \|\varepsilon_N(z)\| < \varepsilon_N. \tag{11}$$

Define $\widehat{\beta}$ as the estimating values of β. The optimal values β^* are usually obtained by employing the least-square algorithm for fast training of ELM, which satisfies

$$\|H(z, w, g)\widehat{\beta} - T\| = \min_{\beta}\|H(z, w, g)\beta - T\|. \tag{12}$$

The estimated output weight $\widehat{\beta}$ can be obtained based on the following equality.

$$\widehat{\beta} = H^{\dagger} T \tag{13}$$

where $H^{\dagger}$ is the Moore–Penrose generalized inverse of the matrix H.

Remark 2. In contrast to its use in tasks like classification or prediction (Berghout et al., 2020), the application of ELM in controller design requires real-time iteration. Consequently, it is essential to utilize an online update law for the subsequent controller design, differentiating it from the solution form of Eq. (13).

3. Controller design

3.1. Overall control structure

To design the controller, the following integral terminal sliding mode surface is defined as follows (Lian et al., 2021).

$$s = \dot{e}_Q + \int_{t_0}^{t} \lambda_1 |e_Q|^{\gamma_1} \operatorname{sign}(e_Q) + \lambda_2 |\dot{e}_Q|^{\gamma_2} \operatorname{sign}(\dot{e}_Q) \mathrm{d}\tau \tag{14}$$

where $e_Q = x_1 - x_d$ denotes the tracking error. λ_1, λ_2, γ_1, and γ_2 are the positive parameters to be designed. sign$(\cdot)$ represents the symbolic function. Moreover, based on the principles of ensuring the system Eq. (15) for $s = 0$ is Hurwitz, the γ_1 and γ_2 can be designed to satisfy Eq. (15) to make the sliding variable differentiable.

$$\begin{cases} \gamma_1 \in (0, 1) \\ \gamma_2 = 2\gamma_1/(\gamma_1 + 1) \end{cases} \tag{15}$$

For $r > 0$, $\forall x \in \mathbb{R}$, $|x|^r \operatorname{sgn}(x)$ is a monotonically increasing smooth function (Lian et al., 2021). Based on the sliding mode surface, we have

$$\dot{s} = -a_n \dot{x} - b_n x + c_n u + d_t - \ddot{Q}_d + \lambda_1 |e_Q|^{\gamma_1} \operatorname{sign}(e_Q) + \lambda_2 |\dot{e}_Q|^{\gamma_2} \operatorname{sign}(\dot{e}_Q). \tag{16}$$

Considering the uncertainty of parameters and external disturbance, d_t is generally unknown during drug injection. Depending on the powerful nonlinear learning ability of NN, the ELM can be used to estimate the overall disturbance d_t to improve the control performance. According to the theory of ELM, the input weights and bias are randomly generated, and only the output weights need to be trained during the closed-loop control process. Different from conventional ELM by solving offline, the output weight $\beta \in \mathbb{R}^{N_h \times 1}$ is adaptively updated online. Thus, the nonlinear uncertain term $\widehat{d}_t(z, \beta)$ is estimated by ELM approximator

$$\widehat{d}_t(z, \beta) = h(z)\widehat{\beta} \tag{17}$$

where $z = [e_Q, \dot{e}_Q, Q_d, \dot{Q}_d]^{\mathrm{T}}$ and $h(z) \in \mathbb{R}^{N_h \times 1}$ denote the input vector and the output of the hidden layer, respectively. In this paper, the input weight and bias are chosen randomly within the range $[-1, 1]$ and $[0, 1]$. As the approximation property of the ELM, the nonlinear disturbance term $\widehat{d}_t(z, \beta)$ can be approximated on an appropriate compact set. The output weight β^* is calculated by

$$\begin{aligned} &\beta^* = \operatorname{argmin}\{\sup_{z \in Z}|d_t(z, \beta^*) - \widehat{d}_t(z, \widehat{\beta})|\} \\ &\text{s.t. } d_t(z, \beta^*) = h(z)\beta^* + \varepsilon_N \end{aligned} \tag{18}$$

where ε_N represents the approximated error in $\forall z \in Z$, which is bounded by $|\varepsilon_N| \leq \eta_N$, η_N is a positive unknown constant.

Without considering the nonlinear uncertain term, based on Eq. (16) with $\dot{s} = 0$, we can obtain the following equivalent control input

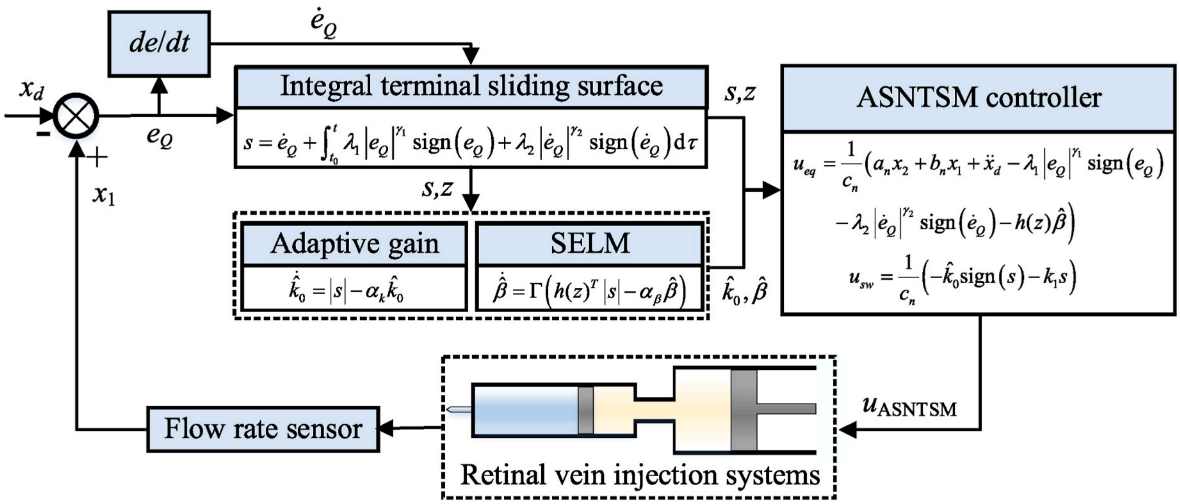

Fig. 3. The block diagram of overall control system.

$$u_{eq}=\frac{1}{c_n}\left(a_n x_2+b_n x_1+\ddot{x}_d-\lambda_1|e_Q|^{\gamma_1}\operatorname{sign}(e_Q)-\lambda_2|\dot{e}_Q|^{\gamma_2}\operatorname{sign}(\dot{e}_Q)-h(z)\hat{\beta}\right) \tag{19}$$

where $\hat{\beta}$ is the adaptive weight related to the uncertainties. Furthermore, a reaching control input with adaptive switching gain is obtained as follows.

$$u_{sw}=\frac{1}{c_n}(-\hat{k}_0\operatorname{sign}(s)-k_1 s) \tag{20}$$

where k_1 is the control gain to be selected. $\hat{k}_0$ is the adaptive gain related to the estimation error η_N of ELM. $\hat{k}_0$ and $\hat{\beta}$ are updated by the following adaptive update laws:

$$\dot{\hat{k}}_0=|s|-\alpha_k\hat{k}_0 \tag{21}$$

$$\dot{\hat{\beta}}=\Gamma\left(h(z)^T|s|-\alpha_\beta\hat{\beta}\right) \tag{22}$$

where α_k, Γ, and α_β are positive constants. By summing up the equivalent and reaching control laws, the overall control input is derived as

$$u_{ASNTSM}=u_{eq}+u_{sw}. \tag{23}$$

Remark 3. The integral sliding surface in Eq. (14) can increase sensitivity to the uncertainties and measurement noise, thereby increase the chattering effect. However, thanks to the design of the ELM, disturbances can be estimated without prior information. With the adaptive gain design, estimation error can be adaptively compensated for while reduce chattering. Additionally, chattering can be further reduced through appropriate parameter selection and smoothing of the sign function. These techniques are further detailed in Section 3.2 and 4.4.

Remark 4. Based on Eq. (21) and the initial condition $\hat{k}_0(0)$, we can obtain $\hat{k}_0(t)=\exp(-\alpha_k t)\hat{k}_0(0)+\int_0^t\exp(-\alpha_k(t-\tau))|s|d\tau>0$, ensuring that the adaptive gain remains greater than zero (Su et al., 2022). In the designed adaptive gain law given by Eq. (21), the first term increases the gain in proportion to the magnitude of the sliding mode variable, thereby enhancing robustness against disturbances. The second term, on the other hand, reduces the gain as the sliding mode variable approaches the sliding surface. By combining these two terms, overestimation of the adaptive gain can be avoided and the chattering effect can be reduced.

Remark 5. The main features of the proposed method are that the integral terminal sliding mode surface of Eq. (14) is adopted to design the control law, which can achieve smaller tracking error and faster convergence speed (Zheng et al., 2014). Then, the overall disturbance of the retinal vein injection system is compensated by the ELM, and the approximate error of the ELM is further estimated by adaptive gain based on Eq. (20). The overall ASNTSM control scheme is shown in Fig. 3.

3.2. Self-evolving mechanism design

The self-evolving mechanism consists of two distinct phases: growing and pruning. During the growing phase, a neuron is added when the specified growth condition is met. Conversely, during the pruning phase, a neuron is removed when the specified pruning condition is satisfied. The specific details are as follows.

3.2.1. Growing phase

During the tracking process, we aim to add neurons in instances where the control error is significant to offset the decrease in control performance resulting from uncertainty. Given the complexity of the judgment error at each sampling moment and its susceptibility to noise, inspired by Qiao et al. (2022), we utilize the mean absolute error (MAE) as the basis for judgment. High values of the MAE indicate poor performance, while low MAE values are associated with achieving good performance. In this paper, a periodic MAE is used to measure the tracking error with a pre-defined time interval ΔT, which can be described as

$$\mathrm{MAE}(i)=\frac{1}{N_t}\sum_{t=(i-2)\cdot\Delta T+\Delta t}^{(i-1)\cdot\Delta T}|e(t)| \tag{24}$$

where N_t represents the number of samples during time interval ΔT. Specially, $\mathrm{MAE}(0)=0$ and $\mathrm{MAE}(1)=e(0)$. Based on MAE, the growth mechanism is triggered when the following conditions are met:

$$\begin{cases}\mathrm{MAE}(i)>\varepsilon_0\\ \mathrm{MAE}(i)-\mathrm{MAE}(i-1)>\varepsilon_1\end{cases} \tag{25}$$

where ε_0 and ε_1 are the predefined positive parameters. At this time, one hidden layer neuron is added, and the input weight and output weight are generated as follows.

$$w_{N_h+1}=w_g \tag{26}$$

$$\beta_{N_h+1}=\beta_g=0 \tag{27}$$

where the growth input weight $w_g\in\mathbb{R}^m$ is generated randomly.

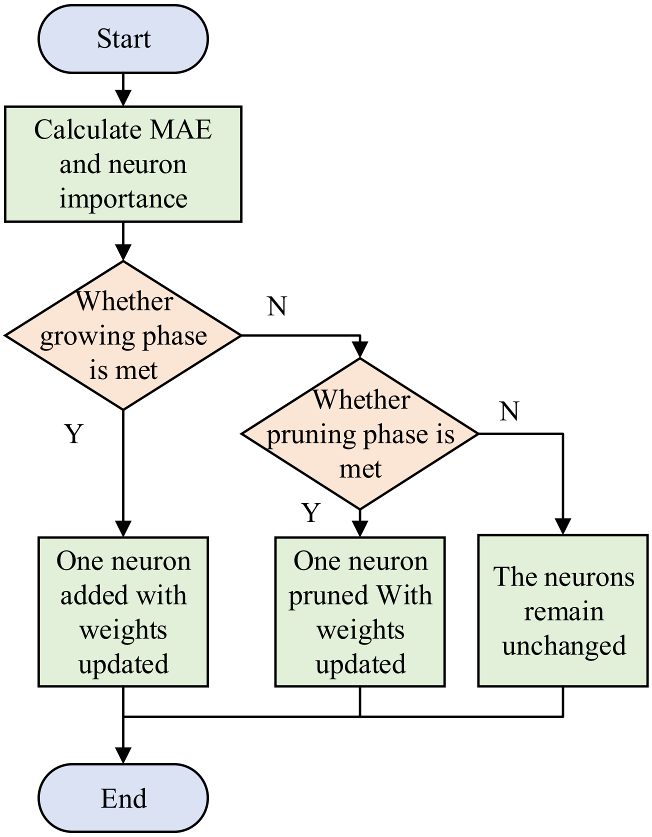

Fig. 4. The flowchart of the self-evolving mechanism.

3.2.2. Pruning phase

We define the importance of the j-th hidden layer neurons at time t:

$$\Xi(j) = \frac{|\beta_j|}{\sum_{k=1}^{N_h}|\beta_k|}\left(1 - \frac{1}{N_h - 1}\sum_{l\in S_n, l\neq j}\rho(U_j, U_l)\right) \tag{28}$$

where U_j and U_l represent the output vector of the j-th and l-th output neuron during the time interval ΔT, respectively. $\rho(U_j, U_l)$ represents the correlation coefficient between variables U_j and U_l, and $\rho(U_j, U_l) \in [0, 1]$. So we define the pruning trigger condition as:

$$\begin{cases} \mathrm{MAE}(i) \leq \varepsilon_0 \\ \mathrm{MAE}(i) - \mathrm{MAE}(i-1) \leq \varepsilon_1 \\ \Xi_j = \mathrm{argmin}\left[\Xi_1, \cdots, \Xi_{N_h}\right] < \mu_\Xi - k_\Xi\sigma_\Xi \end{cases} \tag{29}$$

where μ_Ξ and σ_Ξ represent the mean and standard deviation of the importance vector of hidden layer neurons, respectively. The pruning condition is inspired by the k-sigma rule in statistical process control (Aradhya et al., 2022). It refers to the level of variability within a specific dataset. The parameter k_Ξ controls the confidence level of the sigma rule, which quantifies the sensitivity for pruning the hidden neurons. When the above pruning conditions are met, the j-th hidden layer neuron will be removed. The input and output weights of ELM will also be updated:

$$w_j = 0 \tag{30}$$

$$\beta'_{j_s} = \beta_{j_s} + \beta_j h_j \Big/ h_{j_s}, \beta_j = 0 \tag{31}$$

where $j_s = \underset{k\notin j}{\mathrm{argmax}}\left[\rho(U_j, U_1), \cdots, \rho(U_j, U_k), \cdots, \rho(U_j, U_{N_h})\right]$ represents the neuron with the strongest correlation to the pruned neuron. β_{j_s} and β'_{j_s} represent the before and after updated output weight of the j_s-th neuron, respectively. h_j and h_{js} represent the hidden layer output of the j-th neuron and the j_s-th neuron when the pruning phase is triggered.

Remark 6. The ELM approximator has the capability to adaptively adjust the hidden layer structure during the closed-loop control process, in accordance with the proposed self-evolving mechanism, thus achieving a more compact structure. In this paper, the initial hidden neuron is chosen as 4, which is consistent with the number of input variables. The flowchart of the self-evolving mechanism within predefined time interval is shown in Fig. 4.

Remark 7. The self-evolving mechanism serves as the structural adjustment rule for ELM, introducing additional computational overhead. The calculation process of the self-evolving ELM primarily consists of three components: weight initialization, updating of the hidden structure, and updating of the output weights. In the first control period, for an ELM with m input nodes and $N_h(0)$ hidden-layer nodes, the computational complexity of weight initialization is $\mathrm{O}(mN_h(0))$. During the fixed triggering period, structure updating mainly involves importance calculation, with a computational complexity of $\mathrm{O}\left(N_h^2(t)\right)$. The computational complexity of the output weight updating is $\mathrm{O}(N_h(t))$ during each control period (Han et al., 2018). It is evident that the computational complexity of the self-evolving ELM is primarily related to $N_h(t)$. Since $N_h(t)$ can be adjusted online according to the control performance and excessive growth is unlikely, its computational complexity does not increase significantly compared to fixed-structure ELM. Therefore, the computational complexity of the self-evolving ELM is affordable, especially when the adjustment frequency of the structure is low.

3.3. Stability analysis

In this paper, we prove the finite-time stability of the retinal vein injection system on the basis of the Lyapunov criterion. Before the stability analysis, the following Lemma 1 is first introduced.

Lemma 1. *(Shao et al., 2021): Given the following first-order nonlinear differential inequality:*

$$\dot{V}(x) + \vartheta V(x) \leq \varpi \tag{32}$$

where $\vartheta > 0$, $\varpi > 0$, and $V(x)$ represents a positive Lyapunov function with respect to the state x, then for any given initial condition $V(x(0)) = V(0)$, the function $V(x)$ converges to the following region

$$V(x) \leq \varpi / \vartheta(1-\theta) \tag{33}$$

in the finite time

$$t \leq \ln(\vartheta(1-\theta)V(0) / \varpi)/\vartheta\theta \tag{34}$$

where $0 < \theta < 1$.

Theorem 1. *Consider the retinal vein injection system* Eq. (7). *By using ASNTSM controller* Eq. (23) *with the adaptive updating laws* Eqs. (21) and (22) *with fixed ELM structure, the sliding variable s, weight estimation error $\widetilde{\beta}$ and switching gain estimation error $\widetilde{k}$ will remain within a small region in finite time.*

Proof. *we consider a Lyapunov function candidate as*

$$V_1 = \frac{1}{2}s^2 + \frac{1}{2}\widetilde{\beta}^T\Gamma^{-1}\widetilde{\beta} + \frac{1}{2}\widetilde{k}_0^2 \tag{35}$$

where $\widetilde{\beta} = \beta^* - \widehat{\beta}$ and $\widetilde{k}_0 = k_0^* - \widehat{k}_0$ denote the estimation errors of ELM weight and switching gain, respectively. Then differentiating with respect to time, it follows that

$$\dot{V}_1 = s\dot{s} - \Gamma^{-1}\widetilde{\beta}^T\dot{\widehat{\beta}} - \widetilde{k}_0\dot{\widehat{k}}_0 \tag{36}$$

Substituting Eq. (16) *into* Eq. (36) *yields*

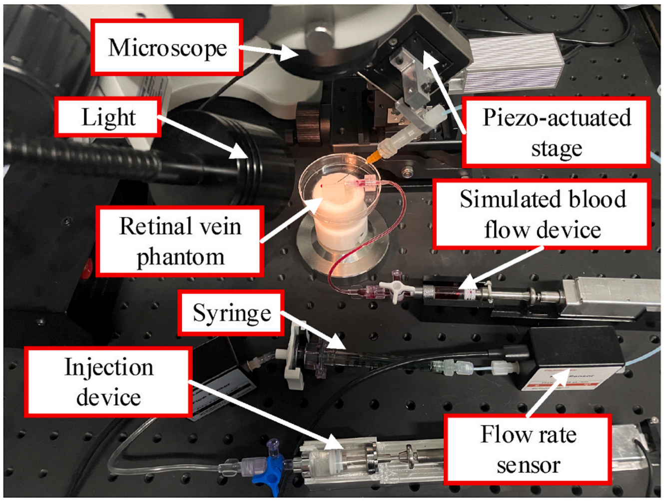

Fig. 5. The retinal vein injection system with silicone phantom.

$$\dot{V}_1 = s\Big(\ddot{e}_Q + \lambda_1 |e_Q|^{\gamma_1}\,\mathrm{sign}(e_Q) + \lambda_2 |\dot{e}_Q|^{\gamma_2}\,\mathrm{sign}(\dot{e}_Q)\Big) - \widetilde{\beta}^T \Gamma^{-1} \dot{\widehat{\beta}} - \widetilde{k}_0 \dot{\widehat{k}}_0$$
$$= s\Big(- a_n \dot{x} - b_n x + c_n u + d - \ddot{x}_d + \lambda_1 |e_Q|^{\gamma_1}\,\mathrm{sign}(e_Q) + \lambda_2 |\dot{e}_Q|^{\gamma_2}\,\mathrm{sign}(\dot{e}_Q)\Big)$$
$$- \widetilde{\beta}^T \Gamma^{-1} \dot{\widehat{\beta}} - \widetilde{k}_0 \dot{\widehat{k}}_0. \tag{37}$$

Substituting the control law Eq. (23) *into* Eq. (37) *yields*

$$\begin{aligned}\dot{V}_1 &= s(- h(z)\widehat{\beta} + h(z)\beta^* - \widehat{k}_0 \mathrm{sign}(s) - k_1 s) - \widetilde{\beta}^T \Gamma^{-1} \dot{\widehat{\beta}} - \widetilde{k}_0 \dot{\widehat{k}}_0 \\ &= s(h(z)\widetilde{\beta} + \eta^* - \widehat{k}_0 \mathrm{sign}(s) - k_1 s) - \widetilde{\beta}^T \Gamma^{-1} \dot{\widehat{\beta}} - \widetilde{k}_0 \dot{\widehat{k}}_0.\end{aligned} \tag{38}$$

According to the adaptive gain law Eq. (21) *and the weight update law* Eq. (22), *we can obtain the following inequality*

$$\begin{aligned}\dot{V}_1 &\le |s| h(z)\widetilde{\beta} + |\eta^*||s| - k_1 s^2 - \widehat{k}_0 |s| - |s| h(z)\widetilde{\beta} - \widetilde{k}_0 |s| + \alpha_\beta \widetilde{\beta}^T \widehat{\beta} + \alpha_k \widetilde{k}_0 \widehat{k}_0 \\ &\le \eta_N |s| - k_1 s^2 - \widehat{k}_0 |s| - \widetilde{k}_0 |s| + \alpha_\beta \widetilde{\beta}^T \widehat{\beta} + \alpha_k \widetilde{k}_0 \widehat{k}_0 \\ &\le - k_1 s^2 + \alpha_\beta \widetilde{\beta}^T \widehat{\beta} + \alpha_k \widetilde{k}_0 \widehat{k}_0.\end{aligned} \tag{39}$$

For any $\nu_\beta > 1/2$, $\nu_k > 1/2$, *one obtains*

$$\alpha_\beta \widetilde{\beta}^T \widehat{\beta} \le - \alpha_\beta (2\nu_\beta - 1)\widetilde{\beta}^T \widetilde{\beta} \,/\, 2\nu_\beta + \alpha_\beta \nu_\beta \beta^{*T} \beta^* \,/\, 2 \tag{40}$$

$$\alpha_k \widetilde{k}_2 \widehat{k}_2 \le - \alpha_k (2\nu_k - 1)\widehat{k}_2^2 \,/\, 2\nu_k + \alpha_k \nu_k k_2^{*2} \,/\, 2. \tag{41}$$

Substituting Eq. (40) *and* Eq. (41) *into* Eq. (39) *yields*

$$\begin{aligned}\dot{V}_1 &\le - k_1 s^2 - \frac{\alpha_\beta (2\nu_\beta - 1)}{2\nu_\beta} \widetilde{\beta}^T \widetilde{\beta} - \frac{\alpha_k (2\nu_k - 1)}{2\nu_k} \widehat{k}_2^2 + \frac{\alpha_\beta \nu_\beta}{2} \beta^{*T} \beta^* + \frac{\alpha_k \nu_k}{2} k_2^{*2} \\ &\le - \psi_1 V_1 + \psi_2\end{aligned} \tag{42}$$

where

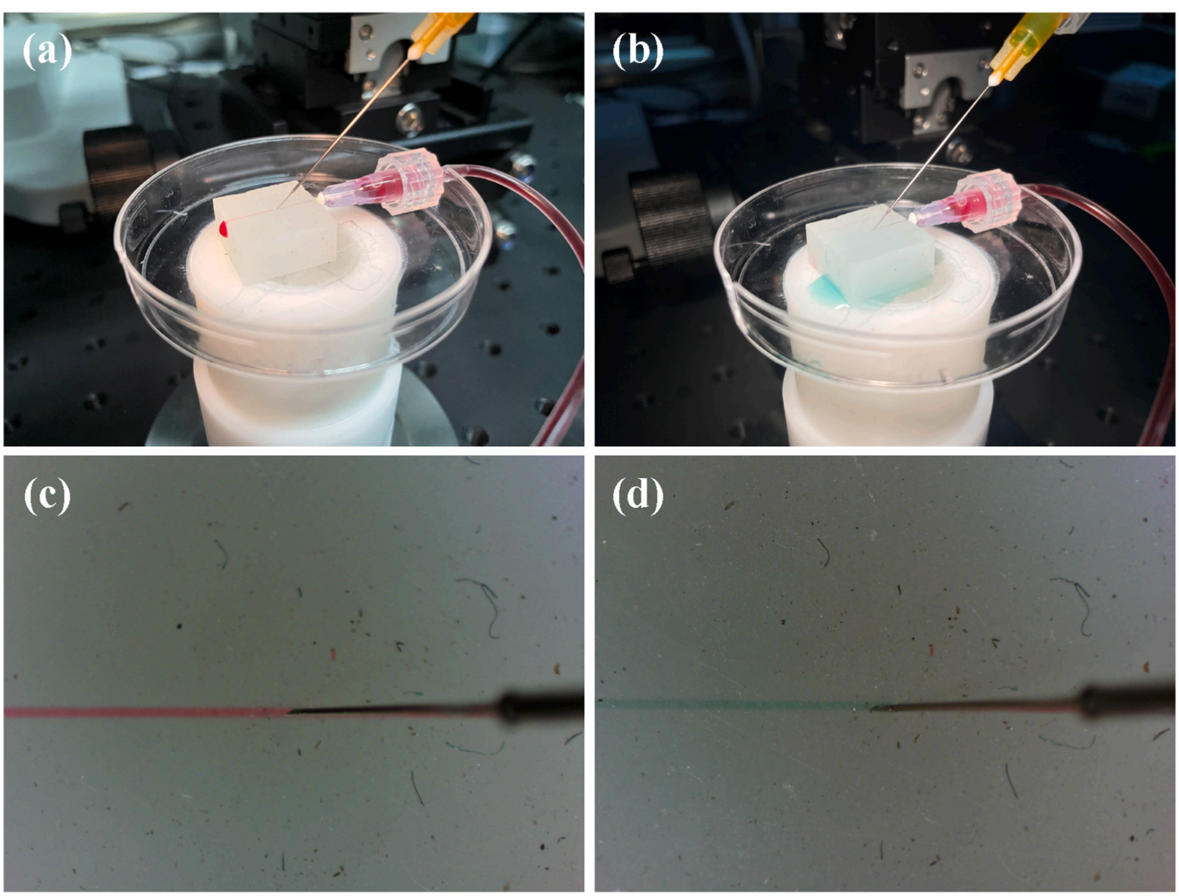

Fig. 6. A retinal vein injection process. (a) The lumen filled with blood without drug injected, (b) The lumen filled with green dyed drug, (c) The microscopic view of the lumen filled with blood, (d) The microscopic view of the lumen filled with drug. (For interpretation of the references to colour in this figure legend, the reader is referred to the Web version of this article.)

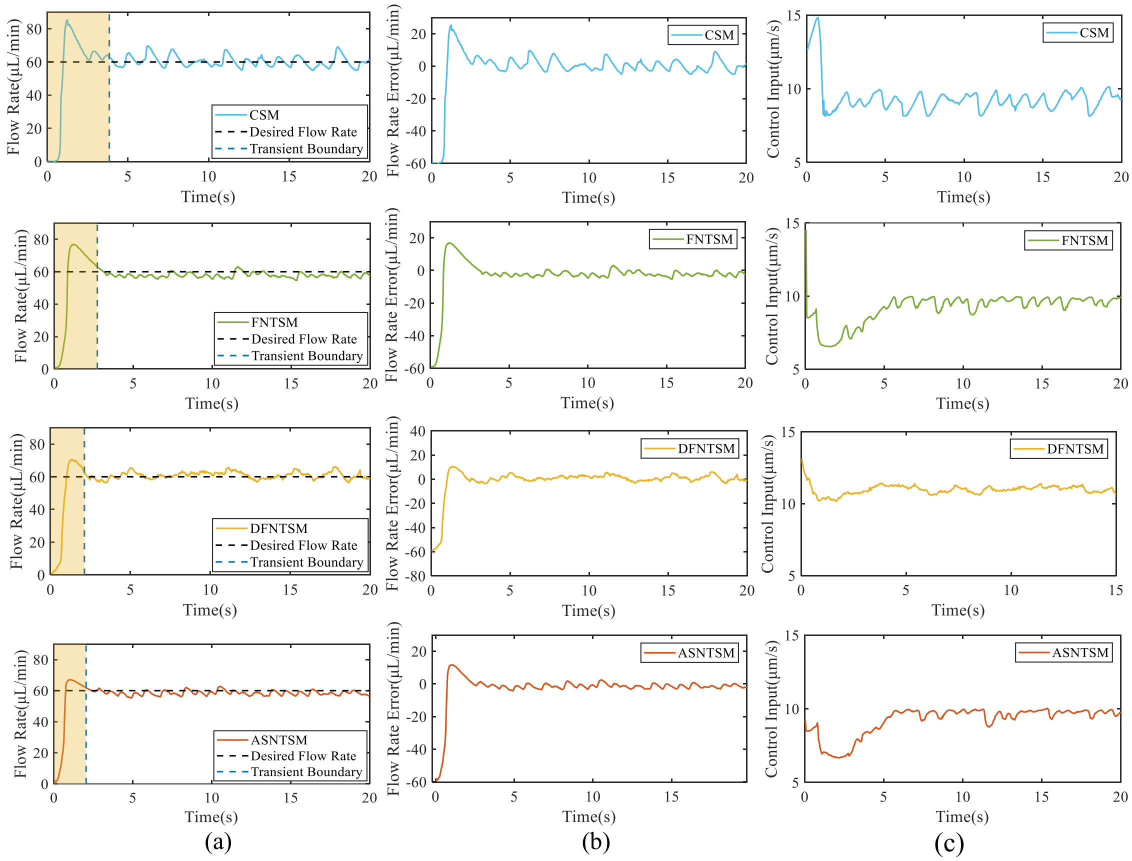

Fig. 7. The experimental results for DFR control without simulated blood flow disturbance. (a) Comparison of set-point control results. (b) Comparison of control errors. (c) Comparison of control inputs.

$$\psi_1 = \min\{2k_1, \alpha_\beta(2\nu_\beta - 1)/\nu_\beta, \alpha_k(2\nu_k - 1)/\nu_k\}, \psi_2 = \frac{\alpha_\beta \nu_\beta}{2}\beta^{*T}\beta^* + \frac{\alpha_k \nu_k}{2}k_2^{*2}.$$

Based on Eq. (42) *and* Lemma 1, *we can conclude that* s, $\widetilde{\beta}$ *and* $\widetilde{k}$ *are bounded and converge to the compact set described as* Eq. (43), *and the finite time is given in* Eq. (44)

$$\begin{aligned} \Omega_s &:= \left\{ s \middle| |s| \le \sqrt{2\psi_2/\psi_1(1-\theta)} \right\} \\ \Omega_{\widetilde{\beta}} &:= \left\{ \widetilde{\beta} \middle| \|\widetilde{\beta}\| \le \sqrt{2\Gamma\psi_2/\psi_1(1-\theta)} \right\} \\ \Omega_{\widetilde{k}_0} &:= \left\{ \widetilde{k}_0 \middle| \sqrt{2\psi_2/\psi_1(1-\theta)} \right\} \end{aligned} \tag{43}$$

$$t_s = \frac{1}{\Psi_1 \theta} \ln\left(V_1(s(0), \widetilde{\beta}(0), \widetilde{k}_0(0)) \frac{\Psi_1(1-\theta)}{\Psi_2} \right). \tag{44}$$

Furthermore, we can prove that the attitude tracking error e_Q converges to zero in a finite time t_s when the sliding mode function $s = 0$. At the sliding surface $s = 0$, Eq. (14) *can be rewritten in the form as*

$$\begin{cases} \dot{x}_1 = x_2 \\ \dot{x}_2 = -\lambda_1 |x_1|^{\gamma_1} \operatorname{sign}(x_1) - \lambda_2 |x_2|^{\gamma_2} \operatorname{sign}(x_2) \end{cases} \tag{45}$$

where $x_1 = e_Q$ and $x_2 = \dot{e}_Q$. It can be proved that the system Eq. (45) *is global finite-time stable* (Zheng et al., 2014)*. From the system* Eq. (45), *there exists a time instance t_s such that $\ddot{e}_Q(t) = 0$ for $t \ge t_s$, therefore, the first derivative of s in* Eq. (14) *is reduced to*

$$\lambda_1 |x_1|^{\gamma_1} \operatorname{sign}(x_1) + \lambda_2 |x_2|^{\gamma_2} \operatorname{sign}(x_2) = 0. \tag{46}$$

According to Yang & Yang (2011), *it can be inferred that* Eq. (46) *for the tracking error $e_Q(t_s)$ can converge to zero in a finite time t_r bounded by*

$$t_r = \frac{2}{1-\gamma_1} \left(\frac{\lambda_2}{\lambda_1} \right)^{\frac{\gamma_1+1}{2\gamma_1}} |e_Q(0)|^{\frac{1-\gamma_1}{2}}. \tag{47}$$

Hence, when $e_Q = 0$ in Eq. (14), *any initial condition $e_Q(0)$ converges to zero in a finite time $t = t_s + t_r$.*

Theorem 2. *Consider the system dynamics as* Eq. (7) *with the control law as* Eq. (23). *When the number of hidden neurons of SELM changes from N_h to $N_h + 1$ with growing phase, and the structure and parameters of the ASNTSM controller are adjusted according to* Eq. (26), *and* Eq. (27). *Then, the stability of the closed-loop system can be also guaranteed with model uncertainties and disturbances.*

Proof. *Considering the hidden layer neurons with the growing phase, we define a Lyapunov function candidate as*

$$V_2 = V_1 + \frac{1}{2}\left(f_g - f_o\right)^2 \tag{48}$$

where f_g and f_o are the outputs of the SELM after and before the growing process, respectively. Then differentiating with respect to time t, we can obtain

$$\begin{aligned} \dot{V}_2 &= \dot{V}_1 + f_g - f_o \\ &= \dot{V}_1 + \sum_{i=1}^{N_h+1} h_i\beta_i - \sum_{i=1}^{N_h} h_i\beta_i \\ &= \dot{V}_1 + \left(h_g\beta_g + \sum_{i=1}^{N_h} h_i\beta_i \right) - \sum_{i=1}^{N_h} h_i\beta_i. \end{aligned} \tag{49}$$

Substituting Eq. (27) *into* Eq. (49) *yields*

$$\dot{V}_2 = \dot{V}_1 \le -\psi_1 V_1 + \psi_2. \tag{50}$$

Similarly, the finite time satisfies $t = t_s + t_r$. Combining with Eqs. (49)–

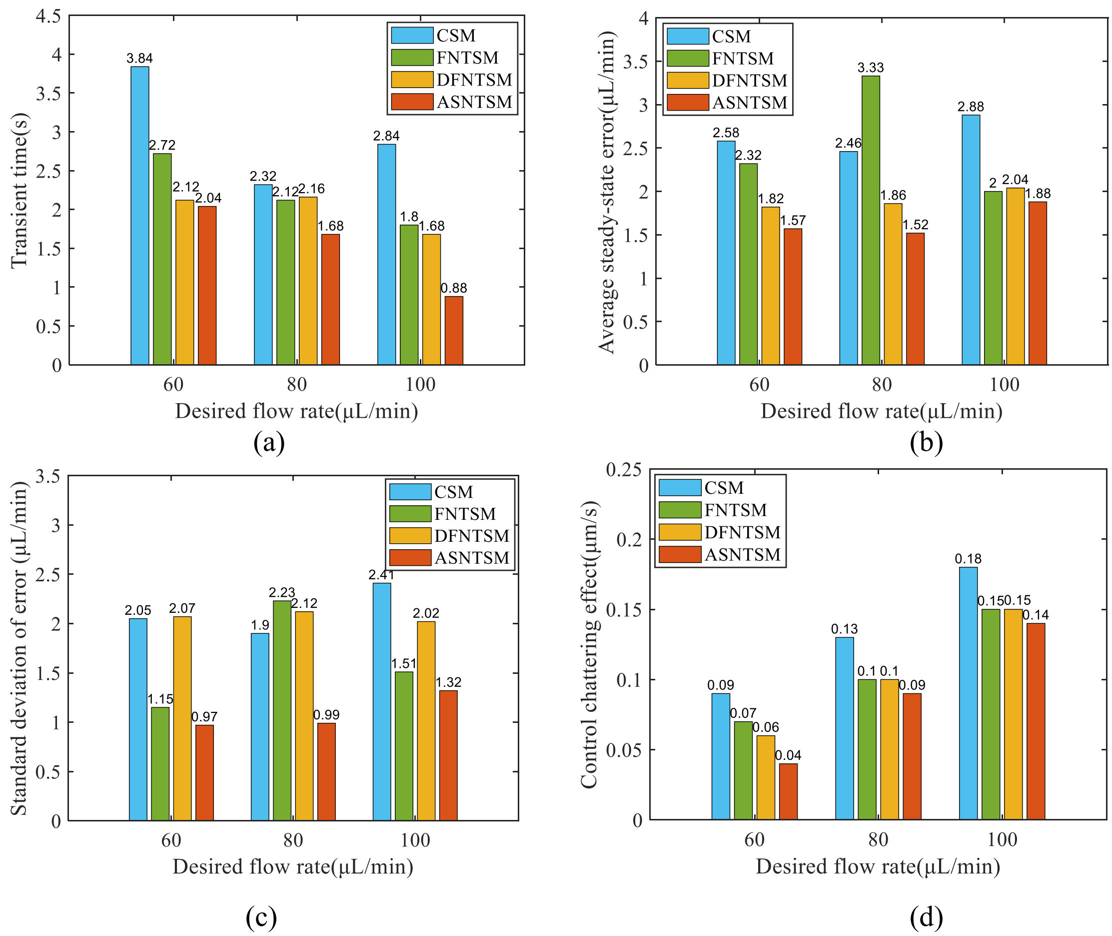

Fig. 8. The performance for DFR control without simulated blood flow disturbance. (a) Transient time. (b) Average steady-state error. (c) Standard deviation of steady-state error. (d) Control chattering effect.

Table 1
The performance improvements of ASNTSM without blood flow disturbance.

Desired flow rate (μL/min)	Method	Improvements (%)			
		Transient time	Average steady-state error	Standard deviation of steady-state error	Control chattering effect
60	CSM	46.88	39.14	52.68	55.56
	FNTSM	25.00	32.33	18.56	42.86
	DFNTSM	3.77	13.74	53.14	33.33
80	CSM	27.59	38.21	47.89	30.77
	FNTSM	20.75	54.35	55.61	10.00
	DFNTSM	22.22	18.28	53.30	10.00
100	CSM	69.01	34.72	45.23	22.22
	FNTSM	51.11	6.00	12.58	6.67
	DFNTSM	47.62	7.84	34.65	6.67
Average	CSM	47.83	37.36	48.60	36.18
	FNTSM	32.29	30.89	28.92	19.84
	DFNTSM	24.54	13.29	47.03	16.67

Table 2
The number of steady-state hidden neurons without blood flow disturbance.

Desired flow rate (μL/min)	60	80	100
Number of steady-state hidden neurons	6	6	7

(51), Theorem 2 *can be proved.*

Theorem 3. *Consider the system dynamics as* Eq. (7) *with the control law as* Eq. (23). *When the number of hidden neurons changes from* N_h *to* $N_h - 1$ *based on the pruning phase, and the structure and parameters of the ASNTSM controller are adjusted according to* Eq. (30) *and* Eq. (31). *Then, the stability of the closed-loop system also can be guaranteed with model uncertainties and disturbances.*

Proof. *Considering the hidden layer neurons with the pruning phase, we define a Lyapunov function candidate as*

$$V_3 = V_1 + \frac{1}{2}\left(f_p - f_o\right)^2 \tag{51}$$

where f_p *and* f_o *are the outputs of the SELM after and before the pruning process, respectively. Then differentiating with respect to time t, we can obtain*

$$\begin{aligned} \dot{V}_3 &= \dot{V}_1 + f_p - f_o \\ &= \dot{V}_1 + \left(\sum_{i=1, i\neq s}^{N_h-2} h_i\beta_i + h_s\beta_s'\right) - \left(\sum_{i=1, i\neq j, i\neq s}^{N_h-2} h_i\beta_i + h_j\beta_j + h_s\beta_s\right) \\ &= \dot{V}_1 + \left(\sum_{i=1, i\neq s}^{N_h-2} h_i\beta_i + h_s\left(\beta_s + \beta_j\frac{h_j}{h_s}\right)\right) - \left(\sum_{i=1, i\neq j, i\neq s}^{N_h-2} h_i\beta_i + h_j\beta_j + h_s\beta_s\right). \end{aligned} \tag{52}$$

Substituting Eq. (31) *into* Eq. (52) *yields*

$$\dot{V}_3 = \dot{V}_1 \leq -\psi_1 V_1 + \psi_2. \tag{53}$$

Similarly, the finite time satisfies $t = t_s + t_r$. *Combining with* Eqs. (51)–

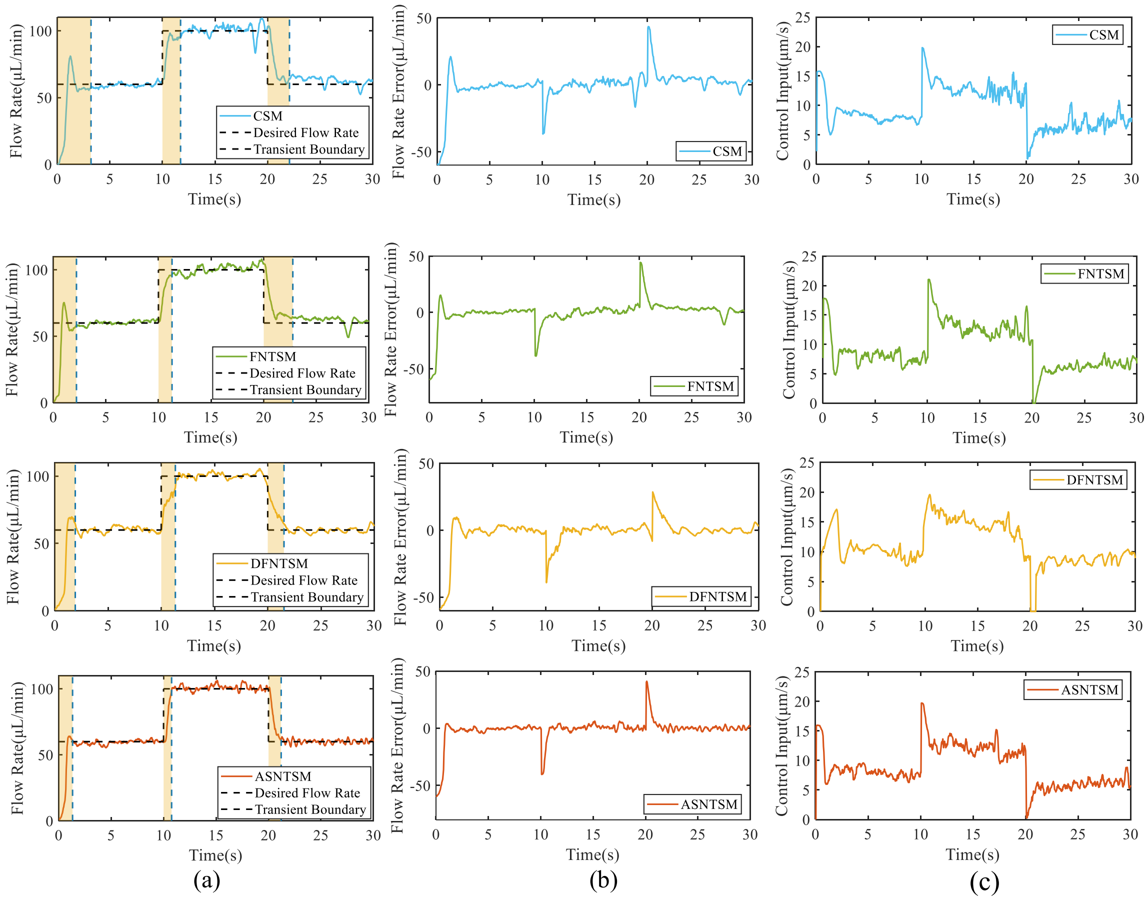

Fig. 9. The experimental results for DFR control with 20 μL/min blood flow rate. (a) Comparison of set-point control results. (b) Comparison of control errors. (c) Comparison of control inputs.

(53), Theorem 3 *can be proved. Therefore, the proposed SELM demonstrates stability even in the presence of uncertainties and disturbances. Furthermore, the tracking error converges to the neighbor of zero in finite-time with ASNTSM controller.*

Remark 8. *The combination of* Theorem 1, Theorem 2, *and* Theorem 3 *demonstrates that the proposed self-evolving mechanism does not impact stability during the control process.*

Remark 9. *Avoiding excessive growth or pruning of the ELM is of significant practical importance. Based on the growth mechanism and* Theorem 1, *the tracking error can converge to zero within finite time as the system reaches steady-state. Select lower values for ε_0 and ε_1 can achieve finite number of hidden neurons. In practical applications, infinite growth is unlikely to occur, as it would require a large and continuously increasing MAE. This can be effectively mitigated through appropriate selection of ε_0 and ε_1. Excessive pruning can only occur when the MAE is small and continuously decreasing, and the third condition in* Eq. (29) *is satisfied. In theory, when the error converges to zero, the pruning mechanism may be triggered in each ΔT period. However, in practice, the third condition of* Eq. (29) *is difficult to meet, as it requires the importance to be below an adaptive threshold (outside the high-confidence interval). Moreover, if the pruning conditions are met and neurons are reduced, it indicates that a large hidden layer is unnecessary. This is also an advantage of the pruning mechanism, which can adaptively reduce computational complexity while maintaining desired precision. To achieve satisfactory structural adjustment, the selection guidelines for ε_0, ε_1, and k_Ξ are further discussed in* Section 3.4.3.

3.4. Guidelines for parameters selection

In the practical implementation of retinal vein injection, the precision of DFR control is influenced by factors such as noise from the flow rate sensor, variations in the retinal vein environment, and the friction of the syringe piston. The ASNTSM controller, when combined with appropriate parameter selection, has the potential to mitigate the aforementioned effects and enhance control performance.

3.4.1. Selection of $\gamma_1, \lambda_1, \lambda_2, k_1$

The parameter γ_1 controls the set-point error of the DFR in the sliding mode variable s. A smaller γ_1 can enhance the responsiveness of the control system, while a larger γ_1 may induce chattering. The parameters λ_1 and λ_2 represent the gains of the integral term in the sliding mode surface. Thanks to the finite-time sliding mode surface, these parameters primarily influence the convergence speed according to Eq. (47). A larger λ_1 decreases the convergence time of the sliding mode variable s, although it may also intensify chattering. Conversely, a smaller λ_2 accelerates convergence while reducing overshoot magnitude. Meanwhile, a larger k_1 expedites convergence but may lead to excessive chattering. Based on the above analysis, we first set $\gamma_1 = 0.6$ to enhance the response speed. Next, we set $\lambda_1 = 25$ to further ensure a fast convergence rate. The values of $\lambda_2 = 0.1$ and $k_1 = 2.5$ are selected to minimize steady-state error while avoiding chattering effects.

3.4.2. Selection of $\Gamma, \alpha_k, \alpha_\beta$

For SELM, a smaller value of Γ enhances the learning speed, but a larger Γ may hinder the convergence of the weights. Meanwhile, a smaller α_β helps mitigate overestimation of the output weights, whereas a larger α_β can lead to unstable updates. Based on these considerations, we select $\Gamma = 0.001$ and $\alpha_\beta = 0.1$.

For adaptive gain, the parameter $\alpha_k > 0$ plays a crucial role in

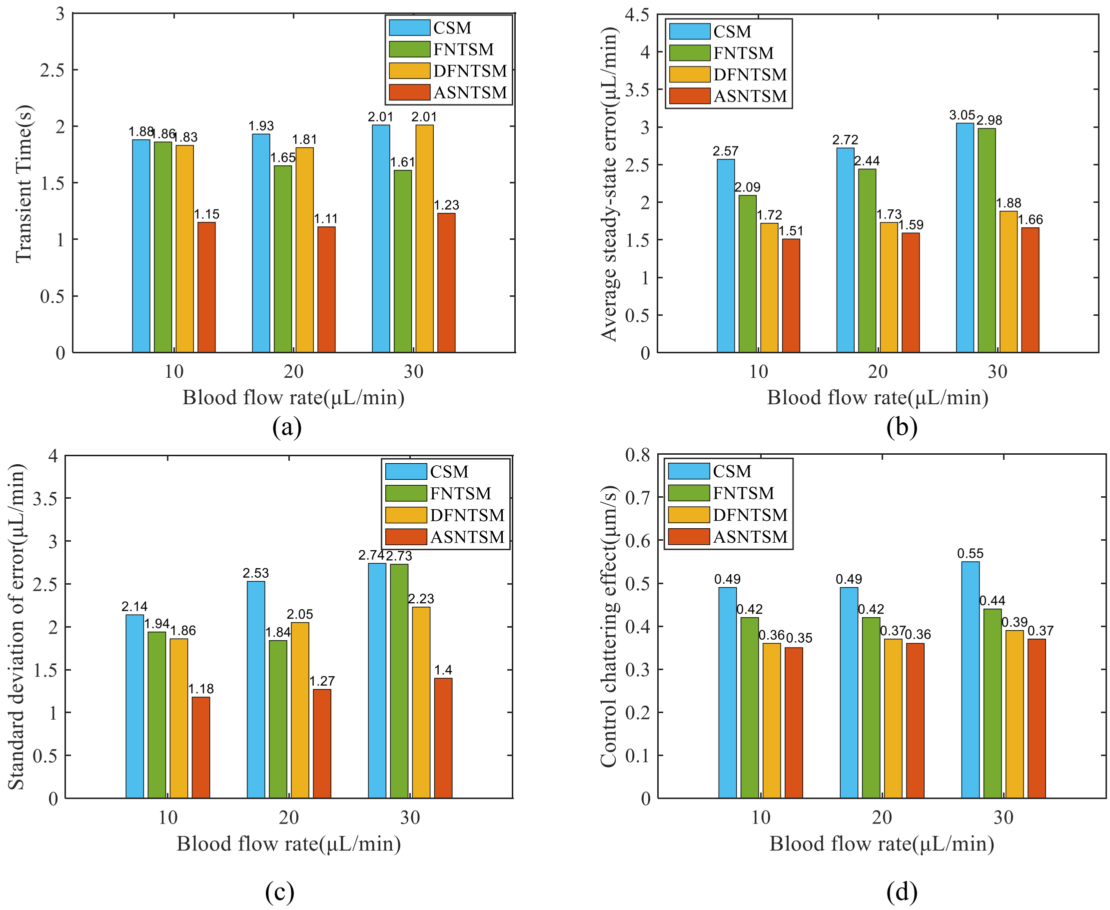

Fig. 10. The performance for DFR control with simulated blood flow disturbance. (a) Transient time. (b) Average steady-state error. (c) Standard deviation of steady-state error. (d) Control chattering effect.

Table 3
The performance improvements of ASNTSM with blood flow disturbance.

Blood flow rate (μL/min)	Method	Improvements (%)			
		Transient time	Average steady-state error	Standard deviation of steady-state error	Control chattering effect
10	CSM	38.83	41.25	44.86	28.57
	FNTSM	38.17	27.75	39.18	16.67
	DFNTSM	37.16	12.21	36.56	2.78
20	CSM	42.49	41.54	49.80	26.53
	FNTSM	32.72	34.84	30.98	14.29
	DFNTSM	38.67	8.09	38.05	2.70
30	CSM	38.80	45.57	48.91	32.73
	FNTSM	23.60	44.30	48.54	15.91
	DFNTSM	38.81	11.70	37.22	5.13
Average	CSM	40.40	42.79	47.86	29.28
	FNTSM	31.50	35.63	39.57	15.62
	DFNTSM	38.21	10.67	37.28	3.54

Table 4
The number of steady-state hidden neurons with blood flow disturbance.

Blood flow disturbance (μL/min)	10	20	30
Number of steady-state hidden neurons	6	7	8

determining the estimation performance. A lower value of α_k allows the adaptive gain to increase more rapidly, which can better compensate for disturbances. However, a larger switching gain may also induce chattering. Conversely, a larger value of α_k can avoid excessive chattering, but the rapidly decreasing gain may struggle to address disturbances effectively, thereby sacrificing control accuracy. Therefore, in the presence of complex disturbances, it is necessary to design a lower α_k to prevent underestimation. In contrast, for constant disturbances, a larger α_k is more suitable to avoid overestimation. Thus, α_k must be carefully selected to balance high precision and reduced chattering. For the retinal vein injection task, the adaptive gain is primarily designed to overcome the estimation error of the ELM. Based on practical performance, $\alpha_k = 0.1$ is selected to achieve high-precision DFR control while simultaneously reducing the chattering effect.

3.4.3. *Selection of* $\Delta\mathrm{T}, \varepsilon_0, \varepsilon_1, \mathrm{k}_\Xi$

The self-evolving mechanism is driven by control performance, with the tracking error and its increment serving as the core criteria for determining the structure updating. the MAE is utilized during the trigger period as the primary rule for adjusting hidden neurons and employ the $k-\sigma$ rule to achieve neuron pruning.

The parameter ΔT determines the time scale for calculating the MAE. A larger ΔT can reduce the fluctuation of the MAE, thereby mitigating the excessive growth of neurons in the SELM. However, it may also cause the structural changes of neurons to lag behind the error fluctuations, potentially leading to a mismatch.

The parameter ε_0 is used to visually determine whether the MAE exceeds the acceptable range. When the MAE is larger than ε_0, it indicates that the number of neurons need to be increased. Conversely, if the MAE is within the acceptable range, neuron growth is deemed unnecessary. A small value of ε_0 makes growth easier, but this also increases the risk of excessive growth. As ε_0 is larger, the growth

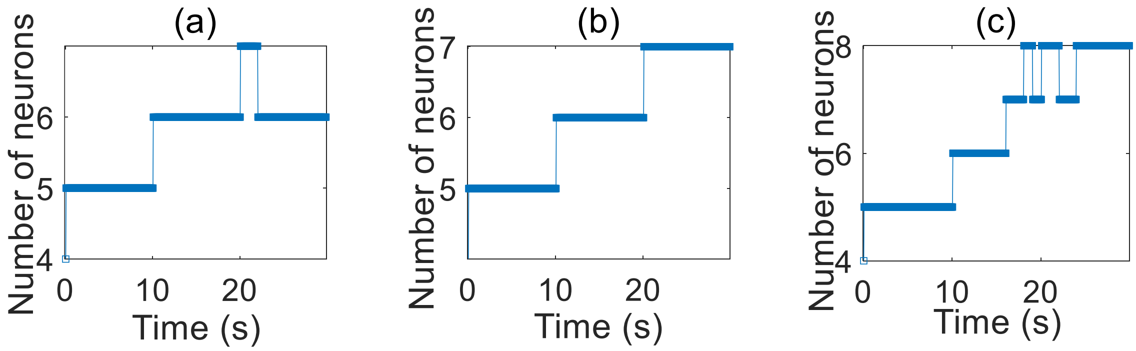

Fig. 11. The hidden neurons of ASNTSM. (a) 10 μL/min blood flow rate. (b) 20 μL/min blood flow rate. (c) 30 μL/min blood flow rate.

mechanism becomes less sensitive to errors. The value of ε_0 must balance control precision with the size of the structure. In scenarios requiring high precision, a smaller ε_0 is necessary to ensure sufficient estimation capability. In other cases, ε_0 can be appropriately increased. It is recommended that the desired error level in experiments be used as a basis for selection. For the retinal vein injection task, we set $\varepsilon_0 = 5$ to achieve appropriate growth capability under disturbances.

The parameter ε_1 determines whether the increment of MAE exceeds the acceptable range. When ε_1 is larger, the growth mechanism becomes less sensitive to the MAE increment. Conversely, a smaller value makes the growth mechanism more sensitive to MAE increments. The value of ε_1 should account for the volatility of the MAE. In the presence of strong fluctuations, a smaller ε_1 can be set to enhance growth ability. In contrast, when fluctuations are smoother, ε_1 can be increased appropriately. It is suggested that the standard deviation of error can be considered as a basis for selection in practical application. For the retinal vein injection task, we set $\varepsilon_1 = 2.5$ to ensure that the adjustment is not overly sensitive to fluctuations.

The role of k_Ξ is to determine whether neurons need to be pruned. This decision is based on the neuron importance as defined by Eq. (28). The $k - \sigma$ rule is used to investigate whether there are neurons with lower information processing capabilities. For example, $(\mu_\Xi \pm \sigma_\Xi)$ defines a region that includes 68 % of all data points as $k_\Xi = 1$. When $k_\Xi = 4$, the interval $(\mu_\Xi \pm 4\sigma_\Xi)$ contains 99.99 % of the data points (Aradhya et al., 2022). The larger the value of k_Ξ, the more difficult it is for neurons to be pruned. Conversely, smaller values of k_Ξ make neurons easier to prune. In scenarios with complex disturbances, more neurons are needed for accurate estimation, and a larger k_Ξ can be considered. In contrast, for scenarios with constant disturbances where excessive neuron growth needs to be inhibited, a smaller k_Ξ is appropriate. Here, we select $k_\Xi = 2$ (contains 95.45 % of the data points) to achieve an acceptable pruning process. This choice ensures sufficient estimation capability to cope with the disturbances in the retinal vein injection system.

Remark 10. For practitioners, balancing fast convergence with the suppression of the chattering phenomenon is crucial. The sliding mode parameters (such as λ_1 and λ_2) primarily influence the convergence speed, while the switching gain parameter α_k mainly affects the chattering phenomenon. To achieve a balance between convergence speed and chattering suppression, it is recommended to first select the parameters related to the sliding mode surface. Specifically, choosing a larger λ_1 and a smaller λ_2 can achieve faster convergence while avoiding obvious chattering. These parameters can then be gradually adjusted as needed. Subsequently, the switching gain parameter α_k should be fine-tuned to reduce gain overestimation and minimize chattering adaptively. Currently, it is challenging to theoretically determine parameters that can simultaneously achieve fast convergence and minimal chattering. However, by combining the above guidelines with experimental trial-and-error, practitioners can iteratively adjust the parameters to find an optimal balance between convergence speed and chattering suppression.

Remark 11. The reduction of chattering can also be achieved through intelligent optimization methods, including particle swarm optimization (Gonzales-Zurita et al., 2023), genetic algorithm (Song et al., 2022). These methods are expected to reduce chattering preserving a faster response speed. By designing a fitness function that incorporates both convergence speed and chattering indicators, the optimized controller parameters can be iteratively refined. Importantly, this approach can significantly reduce the complexity associated with manual parameter selection. In future studies, it is feasible to adopt these intelligent optimization methods to maintain better response speed while minimizing chattering.

4. Experiment

4.1. Platform description

The overall retinal vein injection system is shown as Fig. 5. Initially, a piezo-actuated stage (Scanner65-x. SP-NK, MultiFields Tech) with a maximum displacement of 300 μm, is employed to achieve the axial puncture of the injection needle. The puncture and injection state can be observed within the microscope (MSD204, Murzider) field of view when illuminated by the light source (BG-II, WSoptics).

To achieve precise control of the DFR, a liquid-driven injection system has been developed (Xu et al., 2024). Fig. 5 illustrates the equipment layout of the retinal vein injection system, which includes the injection device (for silicone oil injection), the syringe (for drug injection), and the flow sensor (for real-time feedback). The injection device, based on a brushless micro servo electric cylinder (BLACF30-C112, INSPIRE-ROBOTS), is connected to the syringe via a pressure pipeline. The syringe is connected to the flow sensor (SENSIRION-SLI-1000, Fluidclab) through a pipeline, and the pipeline is connected to the microneedle. In this system, the syringe is filled with the drug, while the back end of the syringe, the pressure pipeline, and the injection device are filled with silicone oil. During injection, the driving mechanism pushes the piston of the injection device forward at a speed (control law), applying pressure to the silicone oil, which in turn pushes the syringe piston to inject the drug. This liquid-driven mechanism significantly reduces the load on the retinal surgery equipment. Another same device (simulated blood flow device in Fig. 5) serves to mimic blood flow for filling the vein lumen. The BD syringe has a total capacity of 1 mL, and the outer diameter of the injection tip measures 100 μm (41G, INCYTO).

A customized silicone phantom with dimensions of 15 mm × 15 mm × 7.5 mm is produced to simulate retinal veins (Shenzhen Phenix Tech). The silicone phantom contained cavities with diameters of 120 μm, 150 μm and 180 μm to simulate retinal veins. The thickness of the vascular cavity from the silicone upper surface is 20 μm. The injection water is a green dyed drug (Indocyanine Green).

4.2. Experimental setup

The controller of the injection system is programmed within the LABVIEW environment on the host computer. The sampling interval is 40ms. Based on the dynamics model of the injection system as described by Eq. (7), the system parameters are identified by the system identification toolbox in MATLAB: $a_n = 2.6$, $b_n = 6$, $c_n = 46.79$. In this paper, the conventional SM (CSM) controller (Utkin et al., 2020), the fast non-singular TSM (FNTSM) controller (Lian et al., 2021), and the disturbance-observer-based FNTSM (DFNTSM) controller are used for comparison experiments. For the CSM controller, the control law is given as:

$$u_{CSM} = \frac{1}{c_n}(a_n\dot{x} + b_n x - C\dot{e} - k_1\sigma - k_2\mathrm{sgn}(\sigma)) \tag{54}$$

where the sliding mode surface of the CSM controller is selected as $\sigma = \dot{e} + Ce$;

For the FNTSM controller, the control law is given as:

$$u_{FNTSM} = \frac{1}{c_n}(a_n x_2 + b_n x_1 - \lambda_1 |e_Q|^{\gamma_1}\mathrm{sign}(e_Q) - \lambda_2 |\dot{e}_Q|^{\gamma_2}\mathrm{sign}(\dot{e}_Q) - k_1 s - k_2\mathrm{sgn}(s)) \tag{55}$$

where the sliding mode surface of the FNTSM controller is as same as Eq. (14). For the DFNTSM controller, the control law is given as:

$$\begin{aligned} u_{DFNTSM} = \frac{1}{c_n}(&a_n x_2 + b_n x_1 - \widehat{d}_t - \lambda_1 |e_Q|^{\gamma_1}\mathrm{sign}(e_Q) \\ &- \lambda_2 |\dot{e}_Q|^{\gamma_2}\mathrm{sign}(\dot{e}_Q) - k_1 s - k_2\mathrm{sgn}(s)) \end{aligned} \tag{56}$$

The $\widehat{d}_t$ is estimated by the disturbance observer, a widely used observer in engineering applications to enhance system robustness (Ding et al., 2020):

$$\begin{cases} \dot{p} = -Lg_2 p - L(g_2 Lx + f + g_1 u) \\ \widehat{d}_t = p + Lx \end{cases} \tag{57}$$

where $x = [x_1, x_2]^T = [Q_2, \dot{Q}_2]^T$, $f = [x_2, -a_n x_2 - b_n x_1]^T$, $g_1 = [0, c_n]^T$, $g_2 = [0, 1]^T$ $L > 0$ is the observer gain. p denotes the internal state of the observer. The parameter selection for ASNTSM is described in detail in Section III. The parameters setting for the CSM controller are: $C = 2.5$, $k_1 = 2.5$, $k_2 = 5$. The parameters setting for the FNTSM controller are: $\gamma_1 = 0.6, \lambda_1 = 25, \lambda_2 = 0.1, k_1 = 2.5, k_2 = 5$. The parameters setting for the DFNTSM controller are: $k_1 = 2.5$, $k_2 = 5$, $L = [8, 0.1]$. The four sliding mode controllers adopt hyperbolic tangent functions instead of sign functions to smooth control signal. The sigmoid activation function is utilized in the experiments, ensuring the nonlinear estimation capability of the SELM for handling disturbances.

In this paper, the transient time, average steady-state error, standard deviation of steady-state error and control chattering effect are used to quantitatively analyze the control performance. The transient time is defined as the time interval from the beginning of injection to the arrival of steady state. The steady state is defined as the point where the DFR tracking error is less than 5 % of the desired value. The shorter the transient time, the faster the response of the retinal vein injection system. The average steady-state error and the standard deviation of steady-state error describe the control accuracy and its stability. The control chattering effect (CCE) is defined as the average absolute value of the control input difference in adjacent control periods:

$$\mathrm{CCE} = \frac{1}{T}\sum_{i=1}^{T} |u(k_c) - u(k_c - 1)| \tag{58}$$

where $|\cdot|$ represents the absolute value, T represents the total control period, and k_c represents the k_c-th control period.

The needle, affixed to the piezo-actuated stage, pierces the wall of the retinal vein to enable continuous infusion of the green dyed drug. An example of drug injection process is provided. As illustrated in Fig. 6, the fluid inside the lumen of the silicone phantom is observable both before and after a successful injection. The lumen of the retinal vein is successfully flushed with green dyed drug.

4.3. Experiment case 1: DFR tracking without simulated blood flow disturbance

In this case, a green dyed drug was injected containing static simulated blood. Three desired DFR set-points are considered to compare the performance of the four sliding mode controllers, which are 60 μL/min, 80 μL/min, and 100 μL/min.

Fig. 7 shows the experimental results of four SM controllers tracking the desired flow rate of 60 μL/min, the detailed responses of the control law are shown Fig. 7(c). Fig. 8 shows the detailed performance of four SM controllers tracking three set-points. Tables 1 and 2 shows the improvement performance of four SM controllers tracking three set-points and number of steady-state hidden neurons, respectively.

In terms of convergence speed, it can be intuitively seen from Fig. 7 (a) that the ASNTSM controller can converge to the steady-state faster than the other three controllers. The ASNTSM controller has less overshoot, reducing the risk of retinal tissue damage during RVC. Based on Table 1, for the three desired flow rate, the transient time of the ASNTSM controller is on average 47.83 % and 32.29 % faster than the CSM, FNTSM, and DFNTSM. The results based on Fig. 8(a) and Table 1 show that the finite-time terminal sliding mode surface can improve the response time, and the SELM further improves the response speed. The ASNTSM controller is more effective than other controllers in reducing transient processes with higher surgical efficiency.

According to Fig. 8(b) and Table 1, the average steady-state error of the ASNTSM controller is on average 37.36 %, 30.89 %, and 13.29 % accurate than the other three controllers.The disturbance observer can compensate for disturbances during the start-up phase, resulting in improved average steady-state error compared to both CSM and FNTSM (average improvement of 27.65 % and 25.1 %). However, due to the uncertainties associated with syringe piston, the improvement in steady-state performance relying on the model-based disturbance observer is limited. Thanks to the combination of TSM and SELM, the control precision of the ASNTSM is significantly better than other methods. Based on Table 1, the standard deviation of steady-state error of the ASNTSM controller is on average 48.6 %, 28.92 %, and 47.03 % stable than the other three controllers. Thus, in the steady-state phase, the ASNTSM controller has higher tracking precision and more stable DFR.

Compared with CSM, FNTSM, and DFNTSM, the control chattering effect of ASNTSM is reduced by 36.18 %, 19.84 %, and 16.67 % respectively. This phenomenon shows that the SELM compensation reduces the overestimation of the switching gain in ASNTSM, thus reducing the chattering effect. In addition, it can be seen from Table 2 that the self-evolving mechanism enables ELM to automatically determine the number of hidden neurons without manually experience. In summary, ASNTSM controller can achieve faster convergence speed, higher control accuracy, more stable performance and less control effect without simulated blood flow disturbance.

4.4. Experiment case 2: DFR tracking with simulated blood flow disturbance

The blood flow within the retinal vein has the potential to disrupt the consistent infusion of the drug. In the experiment, the variable of simulated blood flow rate is set at 10 μL/min, 20 μL/min, and 30 μL/min to evaluate the control performance of the proposed method (Takahashi et al., 2019). To verify the performance of the ASNTSM under simulated blood flow disturbance, the DFR set-point with step change can be described as follows.

$$Q_d(t) = \begin{cases} 60\mu\text{L/min}, & t \leq 10s \\ 100\mu\text{L/min}, & 10s < t \leq 20s \\ 60\mu\text{L/min}, & 20s < t \leq 30s \end{cases} \tag{59}$$

In addition, three different retinal vein diameters are used for each simulated blood flow experiment, and the control result is an average value under three diameters. Fig. 9 shows the experimental results of three SM controllers tracking the variant set-point, the detailed responses of the control law are shown Fig. 9(c). Fig. 10 shows the detailed performance of four SM controllers with variant set-points. Table 3 shows the performance improvement of four SM controllers under simulated blood flow disturbance.

As shown in Fig. 9(a), the ASNTSM controller has the most effective overshoot suppression in the start-up phase compared to the other three SM controllers. Based on Fig. 10(b) and Table 3, the response capability of ASNTSM is also significantly improved, which is not only the selection of terminal sliding mode surface, but also thanks to the addition of SELM, effective NN compensation finally improves the response speed of the ASNTSM. This gives ASNTSM a shorter transient time than FNTSM and DFNTSM, further explaining the need for the framework with TSM and SELM.

From the perspective of control precision, the average steady-state error of ASNTSM is reduced by 42.79 %, 35.63 %, and 10.67 % compared with CSM, FNTSM, and DFNTSM controllers. The CSM and FNTSM controllers have limited ability to overcome the unknown disturbance, so the two controllers cannot accurately track the desired DFR with blood flow disturbance. DFNTSM has the capability of disturbance compensation based on system dynamics. Faced with increased blood flow disturbances, DFNTSM can maintain a stable average steady-state error (from 1.72 μL/min to 1.88 μL/min). However, when confronted with complex disturbances that combine blood flow and piston uncertainties, the accuracy improvement of DFNTSM is insufficient. The ASNTSM controller based on SELM compensation can overcome the disturbance without prior knowledge, thus ensuring the best DFR tracking precision. In the face of complex disturbance, ASNTSM has less steady-error fluctuation than other controllers, which is beneficial for ASNTSM to be applied in more complex clinical scenarios. Although the blood flow disturbance makes the controllers more chattering, the ASNTSM still has a 29.28 %, 15.62 %, and 3.54 % reduction compared to other controllers, which has positive implications for reducing the risk of instability and mechanical damage to the retinal vein injection system.

As shown in Fig. 10(b) and (c), The average steady-state error of ASNTSM remained stable (from 1.51 μL/min to 1.66 μL/min) as the blood flow disturbance increased (from 10 μL/min to 30 μL/min), but increased for both CSM (from 2.57 μL/min to 3.05 μL/min), FNTSM (from 2.09 μL/min to 2.98 μL/min), and DFNTSM (from 1.72 μL/min to 1.88 μL/min). Similarly, the standard deviation of steady-state error for ASNTSM remained stable (from 1.18 μL/min to 1.4 μL/min), but increased for both CSM (from 2.14 μL/min to 2.74 μL/min), FNTSM (from 1.94 μL/min to 2.73 μL/min), and DFNTSM (from 1.86 μL/min to 2.23 μL/min). These results demonstrate the robustness of the ASNTSM, which benefits from the disturbance compensation mechanism of SELM with satisfactory approximation capability.

The designed self-evolving mechanism also circumvents the need to determine the hidden layer structure, resulting in a more compact structure and improved application efficiency of the controller. The numbers of hidden neurons in Table 4 illustrate the self-evolving results of the experiments. Fig. 11 illustrates the specific growth and pruning processes of the SELM. The hidden neurons of SELM remained stable after growth and pruning. The self-evolving mechanism imposes a more stringent condition for pruning compared to that for growth. This helps to mitigate the excessive pruning of neurons in the hidden layer to some extent. Thanks to the approximate ability of the SELM estimator, the disturbance of the injection system can be compensated, and the control performance of ASNTSM is improved.

Overall, the ASNTS controller demonstrates the capability to withstand the disturbance associated with the piston motion during the initial injection, as well as to overcome the disturbance related to the blood flow of retinal vein. Simultaneously, its adaptive ability also confers superior control performance compared to the sliding mode controller with fixed parameters. The design of SELM allows for flexible adjustment of the structure while maintaining satisfactory performance. Consequently, the ASNTSM design is well-suited for the implementation of retinal vein injection tasks. The experimental results demonstrating better tracking accuracy, fast response, and strong robustness.

5. Conclusion

This paper proposes an ASNTSM control strategy to track the desired DFR. To ensure the finite-time tracking performance of the desired DFR, an integral terminal sliding mode control law is designed. To estimate the unknown disturbance from syringe piston friction and the retinal environment, a self-evolving ELM is designed to compensate. The theoretical analysis proved the finite-time stability of the ASNTSM with self-evolving mechanism. The experimental results show that the ASNTSM controller has better tracking speed, accuracy and robustness under variant blood flow disturbances. It is verified that the developed retinal vein injection control system is suitable for clinical RVC surgery.

For future work, it is expected to plan the desired DFR trajectory based on the characteristics of drug-vein interaction, thereby optimize the injection process while reducing the damage on retinal tissue. The application of the desired DFR trajectory and control algorithm is expected further verified in the porcine eyes in vitro.

CRediT authorship contribution statement

Bo Hu: Writing – review & editing, Writing – original draft, Methodology, Formal analysis, Data curation, Conceptualization. **Shiyu Xu:** Writing – review & editing. **Lu Liu:** Methodology. **Rongxin Liu:** Investigation, Data curation. **Mingzhu Sun:** Writing – review & editing, Validation, Supervision, Funding acquisition, Conceptualization. **Xin Zhao:** Writing – review & editing, Validation, Supervision, Funding acquisition, Conceptualization.

Declaration of competing interest

The authors declare that they have no known competing financial interests or personal relationships that could have appeared to influence the work reported in this paper.

Acknowledgement

This research was jointly supported by National Key RD Program of China (2022YFB4702903), Shenzhen Science and Technology Program (JCYJ20240813165501003) and Science and Technology Program of Tianjin (23JCYBJC01240).

Data availability

No data was used for the research described in the article.

References

Annaswamy, A.M., Guha, A., Cui, Y., Tang, S., Fisher, P.A., Gaudio, J.E., 2023. Integration of adaptive control and reinforcement learning for real-time control and learning. IEEE Trans. Automat. Control 68 (12), 7740–7755.

Aradhya, A.M., Ashfahani, A., Angelina, F., Pratama, M., de Mello, R.F., Sundaram, S., 2022. Autonomous CNN (AutoCNN): a data-driven approach to network architecture determination. Inf. Sci. 607, 638–653.

Berghout, T., Mouss, L.H., Kadri, O., Saïdi, L., Benbouzid, M., 2020. Aircraft engines remaining useful life prediction with an adaptive denoising online sequential extreme learning machine. Eng. Appl. Artif. Intell. 96. Article 103936.

Chen, G., Dong, J., 2024. Approximate optimal adaptive prescribed performance Fault-tolerant control for autonomous underwater vehicle based on self-organizing neural networks. IEEE Trans. Veh. Technol. 73 (7), 9776–9785.

Ding, B., Xu, D., Jiang, B., Shi, P., Yang, W., 2020. Disturbance-observer-based terminal sliding mode control for linear traction system with prescribed performance. IEEE Transactions on Transportation Electrification 7 (2), 649–658.

Ding, H., Qiao, J., Huang, W., Yu, T., 2024. Event-triggered online learning fuzzy-neural robust control for furnace temperature in municipal solid waste incineration process. IEEE Trans. Autom. Sci. Eng. 21 (2), 1201–1213.

Dong, H., Yang, X., Gao, H., Yu, X., 2022. Practical terminal sliding-mode control and its applications in servo systems. IEEE Trans. Ind. Electron. 70 (1), 752–761.

Fei, J., Liu, L., 2021. Real-time nonlinear model predictive control of active power filter using self-feedback recurrent fuzzy neural network estimator. IEEE Trans. Ind. Electron. 69 (8), 8366–8376.

Fei, J., Wang, H., Fang, Y., 2021. Novel neural network fractional-order sliding-mode control with application to active power filter. IEEE Transactions on Systems, Man, and Cybernetics: Systems 52 (6), 3508–3518.

Fei, J., Wang, Z., Fang, Y., 2022a. Self-evolving recurrent Chebyshev fuzzy neural sliding mode control for active power filter. IEEE Trans. Ind. Inf. 19 (3), 2729–2739.

Fei, J., Wang, Z., Pan, Q., 2022b. Self-constructing fuzzy neural fractional-order sliding mode control of active power filter. IEEE Transact. Neural Networks Learn. Syst. 34 (12), 10600–10611.

Feng, Z., Liang, W., Ling, J., Xiao, X., Tan, K.K., Lee, T.H., 2022. Precision force tracking control of a surgical device interacting with a deformable membrane. IEEE ASME Trans. Mechatron. 27 (6), 5327–5338.

Fuentes-Alvarez, R., Hernandez, J.H., Matehuala-Moran, I., Alfaro-Ponce, M., Lopez-Gutierrez, R., Salazar, S., Lozano, R., 2022. Assistive robotic exoskeleton using recurrent neural networks for decision taking for the robust trajectory tracking. Expert Syst. Appl. 193, 116482.

Gerber, M.J., Hubschman, J.P., Tsao, T.C., 2021. Automated retinal vein cannulation on silicone phantoms using optical-coherence-tomography-guided robotic manipulations. IEEE ASME Trans. Mechatron. 26 (5), 2758–2769.

Gonzales-Zurita, O., Andino, O.L., Clairand, J.M., Escrivá-Escrivá, G., 2023. PSO tuning of a second-order sliding-mode controller for adjusting active standard power levels for smart inverter applications. IEEE Trans. Smart Grid 14 (6), 4182–4193.

Han, H., Wu, X., Liu, H., Qiao, J., 2018. An efficient optimization method for improving generalization performance of fuzzy neural networks. IEEE Trans. Fuzzy Syst. 27 (7), 1347–1361.

Han, H., Tang, Z., Wu, X., Yang, H., Qiao, J., 2024. Self-organizing broad network with frequency-domain analysis. Eng. Appl. Artif. Intell. 137, 109155.

Helian, B., Mustalahti, P., Mattila, J., Chen, Z., Yao, B., 2022. Adaptive robust pressure control of variable displacement axial piston pumps with a modified reduced-order dynamic model. Mechatronics 87. Article 102879.

Hou, S., Qiu, Z., Chu, Y., Gao, J., Fei, J., 2024a. Hybrid intelligent control using hippocampus-based fuzzy neural networks for active power filter. IEEE Trans. Power Electron. 39 (12), 15924–15942.

Hou, S., Qiu, Z., Chu, Y., Luo, X., Fei, J., 2024b. Robust adaptive learning control using spiking-based self-organizing emotional neural network for a class of nonlinear systems with uncertainties. Eng. Appl. Artif. Intell. 136, 109039.

Huang, G., Huang, G.B., Song, S., You, K., 2015. Trends in extreme learning machines: a review. Neural Netw. 61, 32–48.

Kim, H., Cheon, D., Lim, J., Nam, K., 2019. Robust flow control of a syringe pump based on dual-loop disturbance observers. IEEE Access 7, 135427–135438.

Kitagawa, Y., Shimada, H., Yukita, M., Naruse, S., 2023. Silicone oil injection and removal in 27-gauge vitreous surgery. Int. J. Ophthalmol. 16 (1), 139.

Laouri, M., Chen, E., Looman, M., Gallagher, M., 2011. The burden of disease of retinal vein occlusion: review of the literature. Eye 25 (8), 981–988.

Lian, S., Meng, W., Lin, Z., Shao, K., Zheng, J., Li, H., Lu, R., 2021. Adaptive attitude control of a quadrotor using fast nonsingular terminal sliding mode. IEEE Trans. Ind. Electron. 69 (2), 1597–1607.

Liu, C., Wen, G., Zhao, Z., Sedaghati, R., 2020. Neural-network-based sliding-mode control of an uncertain robot using dynamic model approximated switching gain. IEEE Trans. Cybern. 51 (5), 2339–2346.

Qiao, J., Su, Y., Yang, C., 2022. Online-growing neural network control for dissolved oxygen concentration. IEEE Trans. Ind. Inf. 19 (5), 6794–6803.

Rogers, S., McIntosh, R.L., Cheung, N., Lim, L., Wang, J.J., Mitchell, P., Jonathan Kowalski, W., Nguyen, H., Wong, T.Y., International Eye Disease Consortium, 2010. The prevalence of retinal vein occlusion: pooled data from population studies from the United States, Europe, Asia, and Australia. Ophthalmology 117 (2), 313–319.

Shao, K., Tang, R., Xu, F., Wang, X., Zheng, J., 2021. Adaptive sliding mode control for uncertain Euler–Lagrange systems with input saturation. J. Franklin Inst. 358 (16), 8356–8376.

Song, J., Wang, Y.K., Niu, Y., Lam, H.K., He, S., Liu, H., 2022. Periodic event-triggered terminal sliding mode speed control for networked PMSM system: a GA-optimized extended state observer approach. IEEE ASME Trans. Mechatron. 27 (5), 4153–4164.

Su, X., Xu, Y., Yang, X., 2022. Neural network adaptive sliding mode control without overestimation for a maglev system. Mech. Syst. Signal Process. 168, 108661.

Takahashi, K., Song, Y.S., Sogawa, K., Yoshioka, T., Tani, T., Wada, T., Akiba, M., Sakai, J., Nakamura, S., Minamide, K., Ishiko, S., Yanagi, Y., Yoshida, A., 2019. Characteristics of retinal blood flow, velocity and vessel diameter of eyes with branch retinal vein occlusion as revealed by Doppler optical coherence tomography flowmeter. Investigative Ophthalmology & Visual Science 60 (9), 5727.

Wang, T., Wang, B., Yu, Y., Xu, D., 2022. High-order sliding-mode observer with adaptive gain for sensorless induction motor drives in the wide-speed range. IEEE Trans. Ind. Electron. 70 (11), 11055–11066.

Willekens, K., Gijbels, A., Schoevaerdts, L., Esteveny, L., Janssens, T., Jonckx, B., Feyen, J.H.M., Meers, C., Reynaerts, D., Poorten, E., Stalmans, P., 2017. Robot-assisted retinal vein cannulation in an in vivo porcine retinal vein occlusion model. Acta Ophthalmol. 95 (3), 270–275.

Willekens, K., Gijbels, A., Smits, J., Schoevaerdts, L., Blanckaert, J., Feyen, J.H., Reynaerts, D., Stalmans, P., 2021. Phase I trial on robot assisted retinal vein cannulation with ocriplasmin infusion for central retinal vein occlusion. Acta Ophthalmol. 99 (1), 90–96.

Wu, J., Chui, C.K., Binh, P.N., Teo, C.L., 2013. Real-time Rendering of Drug Injection and Interactive Simulation of Vessel Deformation Using Gpu. In: 2013 35th Annual International Conference of the IEEE Engineering in Medicine and Biology Society (EMBC). IEEE, pp. 4569–4572.

Wu, K., Xu, C., Yan, J., Wang, F., Lin, Z., Zhou, T., 2023. Error-distribution-free kernel extreme learning machine for traffic flow forecasting. Eng. Appl. Artif. Intell. 123. Article 106411.

Xia, Y., Yi, W., Zhang, D., 2022. Coupled extreme learning machine and particle swarm optimization variant for projectile aerodynamic identification. Eng. Appl. Artif. Intell. 114. Article 105100.

Xu, S., Hu, B., Liu, R., Zhao, X., Sun, M., 2024. Liquid-driven microinjection system for precise fundus injection. Sensors 24 (7). Article 2140.

Yang, L., Yang, J., 2011. Nonsingular fast terminal sliding-mode control for nonlinear dynamical systems. Int. J. Robust Nonlinear Control 21 (16), 1865–1879.

Zhang, H., Li, Y., Li, Z., Zhao, C., Gao, F., Xu, F., Wang, P., 2021. Extended-state-observer based model predictive control of a hybrid modular DC transformer. IEEE Trans. Ind. Electron. 69 (2), 1561–1572.

Zhang, H., Wang, C., Bai, M., Yi, H., Yang, J., Zhu, Y., Zhao, J., 2023. A micro-3-degree-of-freedom force sensor for intraocular dexterous surgical robots. Advanced Intelligent Systems 5 (7). Article 2200413.

Zheng, J., Wang, H., Man, Z., Jin, J., Fu, M., 2014. Robust motion control of a linear motor positioner using fast nonsingular terminal sliding mode. IEEE ASME Trans. Mechatron. 20 (4), 1743–1752.